Article

SOURCE DATA | TRANSPARENT PROCESS | OPEN ACCESS

THE EMBO JOURNAL

The EGFR phosphatase RPTPγ is a redox-regulated suppressor of promigratory signaling

Maitreyi S Joshi[1], Angel Stanoev[1,†,‡], Jan Huebinger[1,†], Birga Soetje[1], Veronika Zorina[1], Lisaweta Roßmannek[1], Kirsten Michel[1], Sven AH Müller[1] & Philippe IH Bastiaens[1,2,*]

Abstract

Spatially organized reaction dynamics between proto-oncogenic epidermal growth factor receptor (EGFR) and protein tyrosine phosphatases determine EGFR phosphorylation dynamics in response to growth factors and thereby cellular behavior within developing tissues. We show that the reaction dynamics of mutual inhibition between RPTPγ phosphatase and autocatalytic ligandless EGFR phosphorylation enable highly sensitive promigratory EGFR signaling responses to subnanomolar EGF levels, when < 5% receptors are occupied by EGF. EGF thereby triggers an autocatalytic phospho-EGFR reaction by the initial production of small amounts of phospho-EGFR through transient, asymmetric EGF-EGFR$_2$ dimers. Single cell RPTPγ oxidation imaging revealed that phospho-EGFR induces activation of NADPH oxidase, which in turn inhibits RPTPγ-mediated dephosphorylation of EGFR, tilting the autocatalytic RPTPγ/EGFR toggle switch reaction towards ligandless phosphorylated EGFR. Reversibility of this reaction to EGF is maintained by the constitutive phosphatase activity of endoplasmic reticulum-associated TCPTP. This RPTPγ/EGFR reaction at the plasma membrane causes promigratory signaling that is separated from proliferative signaling induced by accumulated, liganded, phosphorylated EGF-EGFR in endosomes. Accordingly, loss of RPTPγ results in constitutive promigratory signaling from phosphorylated EGFR monomers. RPTPγ is thus a suppressor of promigratory oncogenic but not of proliferative EGFR signaling.

Keywords EGFR-PTP interaction; oncogenic signaling network; PTP oxidation; reactive oxygen species; toggle-switch dynamics
Subject Categories Membrane & Trafficking; Post-translational Modifications & Proteolysis; Signal Transduction
DOI 10.15252/embj.2022111806 | Received 2 June 2022 | Revised 20 February 2023 | Accepted 23 February 2023 | Published online 29 March 2023
The EMBO Journal (2023) 42: e111806

Introduction

The receptor tyrosine kinase EGFR (epidermal growth factor receptor; Cohen *et al*, 1980; Yarden & Schlessinger, 1987) is implicated in embryonic development, tissue homeostasis, and wound healing (Sibilia *et al*, 2007; Yu *et al*, 2010), while EGFR overexpression and hyper-activation through genetic alterations have been linked to malignant transformation (Rowinsky, 2004). On the one hand, it has been established that EGFR can dimerize upon binding of its cognate ligand to relatively stable, phosphorylated dimers of 2:2 EGF-EGFR stoichiometry, which initiate signal transduction (Lemmon *et al*, 1997; Ogiso *et al*, 2002). On the other hand, evidence has accumulated that EGFR is embedded in a spatially–temporally organized protein tyrosine phosphatase (PTP) network (Verveer *et al*, 2000b; Ostman & Böhmer, 2001; Tiganis, 2002; Reynolds *et al*, 2003; Baumdick *et al*, 2015; Stanoev *et al*, 2018), allowing it to sense and differentially respond to evolving growth factors patterns in collective cell responses like tissue regeneration (Hiratsuka *et al*, 2015; Stallaert *et al*, 2018; Hino *et al*, 2020; Brüggemann *et al*, 2021; Lin *et al*, 2022). Here, EGFR operates within a growth factor sensory system that can detect time-varying growth factor patterns by ligand-induced conversion of EGFR monomers to transient dimers (Verveer *et al*, 2000b; Reynolds *et al*, 2003; Chung *et al*, 2010; Low-Nam *et al*, 2011) that catalytically and autocatalytically generate an amplified phosphorylation response in EGFR monomers (Verveer *et al*, 2000b; Reynolds *et al*, 2003; Ichinose *et al*, 2004; Baumdick *et al*, 2018; Stanoev *et al*, 2018; Koseska & Bastiaens, 2020). These ligandless EGFR monomers are dynamically maintained at the plasma membrane (PM) by recycling through the recycling endosomes (REs; Baumdick *et al*, 2015) in contrast to EGF-bound and ubiquitinated EGFR complexes that uni-directionally traffic (Herbst *et al*, 1994; Baumdick *et al*, 2015) from early endosomes (EEs; Vieira *et al*, 1996) to late endosomes (LEs; Vanlandingham & Ceresa, 2009), to be degraded in lysosomes (Levkowitz *et al*, 1998; De Melker *et al*, 2001; Haglund *et al*, 2002; Baumdick *et al*, 2015; Koseska & Bastiaens, 2020). Because of this differential trafficking of liganded phosphorylated EGFR (EGF-EGFRp) and ligandless phosphorylated EGFR monomers (EGFRp), evolving growth factor patterns can generate contextual cellular responses by altering the dynamically

1 Department of Systemic Cell Biology, Max Planck Institute for Molecular Physiology, Dortmund, Germany
2 Faculty of Chemistry and Chemical Biology, TU Dortmund, Dortmund, Germany
*Corresponding author. Tel: +49 0231 1332200; E-mail: philippe.bastiaens@mpi-dortmund.mpg.de
†These authors contributed equally to this work
‡Present address: Janelia Research Campus, Howard Hughes Medical Institute, Ashburn, VA, USA

established spatial distribution of phosphorylated EGFR between the PM and endosomal compartments (Stallaert *et al*, 2018; Brüggemann *et al*, 2021). This is necessary to spatially–temporally coordinate proliferative, differentiating, or migratory cell responses in the context of an evolving tissue. At the PM, (auto)-catalytic activity of phosphorylated EGFR can further phosphorylate more EGFR monomers in the absence of growth factors, requiring PTPs to counter spontaneous phosphorylation of EGFR (Verveer *et al*, 2000b; Tiganis, 2002; Reynolds *et al*, 2003; Tischer & Bastiaens, 2003). In this respect, reciprocal genetic perturbations combined with *in situ* EGFR phosphorylation imaging has identified PM-localized RPTPγ (LaForgia *et al*, 1991) and endoplasmic reticulum (ER) associated TCPTP (Cool *et al*, 1989) as major dephosphorylating activities that regulate the phosphorylation response of EGFR to EGF (Stanoev *et al*, 2018). However, the 2–3 orders of magnitude higher catalytic activity of PTPs with respect to the kinase activity of EGFR (Fischer *et al*, 1991; Lammers *et al*, 1993) suppresses growth factor responses, requiring EGFR-signaling-induced PTP inhibition (Bae *et al*, 1997; Denu & Tanner, 1998) to allow for the observed amplified EGFR phosphorylation response to physiological growth factors levels (Verveer *et al*, 2000b; Reynolds *et al*, 2003; Stanoev *et al*, 2018).

Herein, we address this conundrum by showing that EGFRp-coupled NADPH-oxidase (NOX1-3) activity leads to H_2O_2-mediated oxidation of RPTPγ's catalytic cysteine at the PM thereby enabling an autocatalytic EGFR phosphorylation response to physiological EGF levels, at which less than 5% of the receptors are engaged, and thus, a very low fraction of EGF_2-$EGFR_2$ dimers is created. The inhibition of RPTPγ's inhibitory phosphatase activity on autocatalytically phosphorylated ligandless EGFRp together with its three orders of magnitude lower phosphatase activity on EGF-EGFRp, enables an ultrasensitive EGFR phosphorylation response at the PM to low, subnanomolar EGF levels. RPTPγ's constitutive vesicular recycling through the thiol-reducing environment of the cytoplasm closes the phosphatase de-activating/re-activating redox cycle on RPTPγ, enabling EGFR phosphorylation levels to reset to basal levels in response to declining growth factor concentrations. On the other hand, the constitutive dephosphorylating activity of the PM-proximal pool of ER-associated TCPTP poises autocatalytic EGFR-RPTPγ toggle switch dynamics away from a preactivated state, into an ultrasensitive reversible growth factor response regime. Consistent with EGFR/RPTPγ toggle switch reaction dynamics at the PM, knock-out of RPTPγ leads to maximally attainable ligandless EGFR monomer phosphorylation and a highly morphing migratory phenotype of MCF7 cells. In contrast, knock-out of the NOX1-3 subunit $p22^{phox}$ results in a more stationary cellular behavior together with hyperproliferative growth factor response that stems from proliferative signaling of liganded receptors in endosomes. RPTPγ is thus a suppressor of promigratory oncogenic ligandless EGFR monomer signaling from the PM but not of proliferative cytoplasmic signaling of internalized liganded EGFR.

Results

EGFR phosphorylation response is dependent on NOX and RPTPγ activity

To study the effect of EGFR-induced ROS production on EGFR's phosphorylation response, the essential $p22^{phox}$ (*CYBA*) subunit (Ambasta *et al*, 2004) of the NOX1-4 complexes was knocked out in breast cancer-derived MCF7 cells by CRISPR-Cas9 gene editing (Fig EV1A). MCF7 cells do not express ER-localized NOX4 (Juhasz *et al*, 2009) and their ER-localized NOX5 complex is independent of $p22^{phox}$ (Kawahara *et al*, 2005). Thus, this KO is specific for PM-localized NOX1-3. We measured early (5′) endogenous EGFR tyrosine phosphorylation response (pY1068) as function of EGF dose (0, 20, 80, 160 ng/ml) as well as down-stream Akt and Erk signaling by phospho-amino-acid specific markers for activation (Akt: pS473; Erk: pT202, pY204; Seger *et al*, 1991; Jacinto *et al*, 2006) using quantitative western blot analysis. In WT cells, an abrupt switch in EGFR phosphorylation occurred at 20 ng/ml that stayed maximal up to 160 ng/ml EGF (Figs 1A, left panel and EV1C). This EGF dose-dependent switch was also apparent in the early (5′) down-stream EGF-dependent activation of Akt and Erk (Figs 1A, middle and right panels, and EV1C). This response was, however, completely abolished in $p22^{phox}$-KO cells (clone 11, Fig EV1A), where pY1068 remained at basal (non-stimulated) level, over the whole tested range of EGF dose up to 160 ng/ml (Figs 1A and EV1C). This shows that NOX1-3-induced ROS activity is essential for EGF-induced EGFR phosphorylation as well as down-stream signaling in MCF7 cells. We have previously identified PM-localized RPTPγ as a major EGFR dephosphorylating activity whose catalytic cysteine is sensitive to oxidation by H_2O_2 (Stanoev *et al*, 2018). Concordantly, in MCF7 cells where RPTPγ (*PTPRG*) was knocked-out by CRISPR-Cas9 gene editing (Fig EV1B, clone 14), high EGFR phosphorylation together with high Erk and Akt phosphorylation was found in the absence of stimulus, reaching levels similar to WT cells stimulated with 160 ng/ml EGF (Figs 1B and EV1D). This high-basal level of EGFR, Erk and Akt phosphorylation in RPTPγ KO cells was close to maximal attainable levels as apparent from the marginal elevation upon increasing the dose of EGF (Fig 1B). In a reciprocal experiment in a colorectal cancer cell line (HT29) that is deficient in RPTPγ expression due to promoter methylation (Van Niekerk & Poels, 1999), EGFR phosphorylation was also at a high-basal level and could be significantly lowered by ectopic expression of RPTPγ (Fig EV1E and F). This indicates that RPTPγ is a suppressor of aberrant, autonomous EGFR signaling.

Inhibition of EGFR's kinase activity by gefitinib (10 μM) in both WT, and RPTPγ KO MCF7 cells abolished the phosphorylation of EGFR as well as that of down-stream Akt and Erk (Figs 1C and EV1G). This demonstrates that EGFR phosphorylation in RPTPγ KO MCF7 cells was dependent on EGFR's intrinsic tyrosine kinase activity. Furthermore, homo-FRET fluorescence anisotropy microscopy on an EGFR-QG-mCitrine construct (Baumdick *et al*, 2015) ectopically expressed in MCF7 cells showed that EGFR in unstimulated WT and RPTPγ-KO cells was predominantly monomeric, whereas cells that were stimulated with 160 ng/ml exhibited a higher steady state level of receptor dimers (Fig 1D). Unstimulated RPTPγ KO cells, therefore, contain phosphorylated, monomeric EGFR. These results thereby show that RPTPγ is a major PTP that suppresses spontaneous trans-phosphorylation of EGFR in the absence of stimulus. Furthermore, they show that ligandless, phosphorylated EGFR-monomers can engage down-stream Erk and Akt signaling from the PM.

As unliganded EGFR monomers in the absence of EGF in RPTPγ-KO cells reached the same maximally attainable phosphorylation levels as WT MCF7 cells stimulated with 20 ng/ml EGF for 5′, we

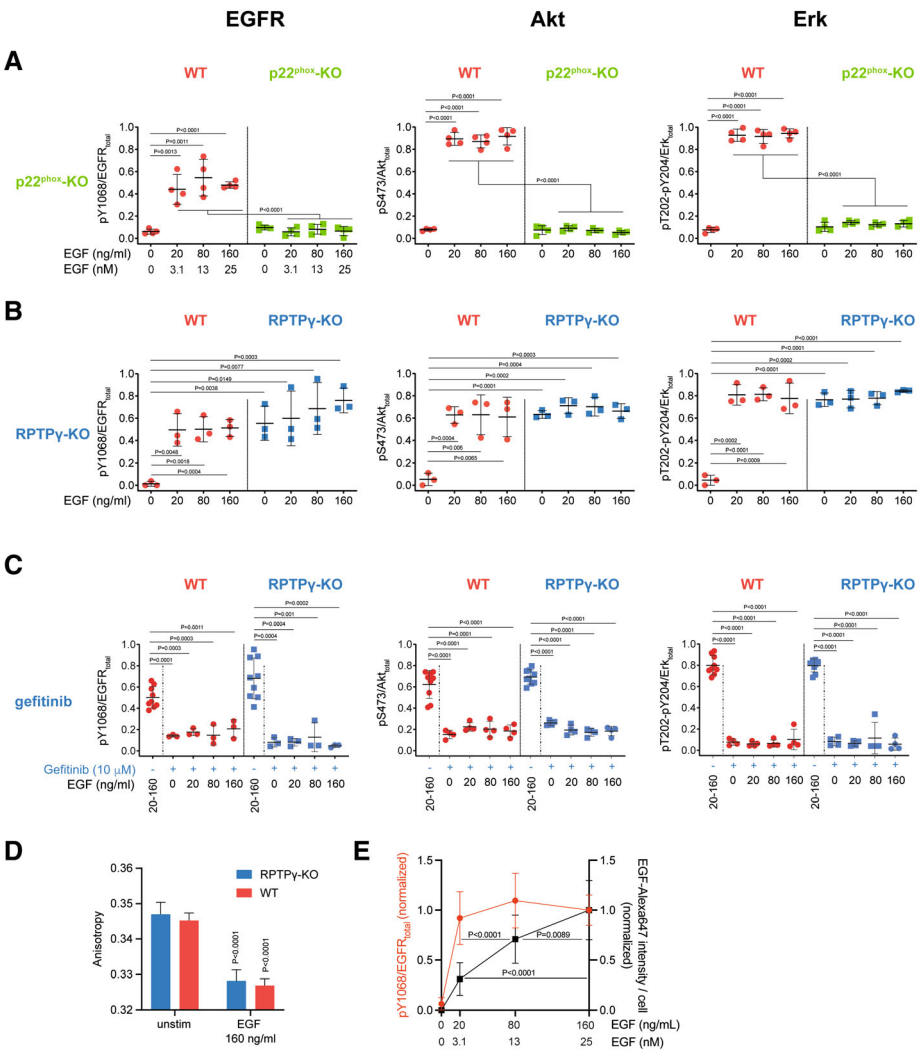

Figure 1. RPTPγ and NOX are essential for EGFR-phosphorylation responses at non-saturating receptor occupancy by EGF.

A EGFR (pY1068, left), Akt (pS473, middle), and Erk (pT202 and pY204, right) phosphorylation response in WT (red) compared to p22^{phox}-KO (green) MCF7 cells as function of EGF concentration (ng/ml; nM) upon 5′ stimulation with different doses of EGF-Alexa647 quantified from Western blot analysis. $N = 4$ biological replicates with mean ± SD, P: unpaired two-tailed *t*-test.

B Same as (A) comparing WT (red) to RPTPγ-KO (blue) MCF7 cells. $N = 3$ biological replicates with mean ± SD, P: unpaired two-tailed *t*-test.

C Quantitative Western blot analysis as in (A) comparing WT (red) and RPTPγ-KO (blue) MCF7 cells after EGF stimulus (20, 80, 160 ng/ml from (B), left column: w/o Gefitinib) to the cells from the corresponding cell line treated with 10 μM of the EGFR-inhibitor Gefitinib for 1 h and the indicated EGF concentration for the last 5′ (ng/ml). $N = 3$ biological replicates with mean ± SD, P: unpaired two-tailed *t*-test.

D Quantification of live cell fluorescence anisotropy microscopy measurements of EGFR-QG-mCitrine dimerization level in WT (red) and RPTPγ-KO (blue) MCF7 cells before and after 160 ng/ml EGF-Alexa647 stimulus for 15′. mean ± SEM, $N = 3$ biological replicates, $n = 31$ cells, P: paired two-tailed *t*-test, against respective unstimulated cases.

E Comparison of normalized EGFR-phosphorylation (pY1068/EGFR$_{total}$) as a function of EGF concentration ($N = 10$, from Figs 1A and B, and EV1E, red) to EGF-Alexa647 bound to WT MCF7 cells at the corresponding, indicated concentrations normalized to the 160 ng/ml, measured by fluorescence microscopy. $N = 5$ biological replicates, $n = 16$–19 fields of view, mean ± SD, P: One-way ANOVA with Tukey's multiple comparison test.

Source data are available online for this figure.

questioned whether this dose is saturating EGFR binding sites and thereby generating 2:2 EGF$_2$-EGFR$_2$ dimers. To assess this, we related EGFR phosphorylation to the fraction EGFR that is bound by EGF (α_L: EGF-EGFR/EGFR) for a given EGF dose within this 5′ time frame. To estimate α_L in the lowly EGFR expressing WT MCF7 cells (Imai *et al*, 1982; Roos *et al*, 1986; Charafe-Jauffret *et al*, 2006), we administered 20, 40, 80, and 160 ng/ml fluorescent EGF-Alexa647 for 5′ to WT MCF7 cells together with Hoechst33342 to mark the nucleus of each cell. After rapidly washing the excess EGF-Alexa647 from the medium, the integrated fluorescence of bound EGF-Alexa647 per cell was measured (Figs 1E and EV1H). This provides a measure of the total amount of EGF that has bound over 5′ to each

cell. An average α_L per cell for a given EGF-Alexa647 concentration was then estimated by normalizing the integrated fluorescence of EGF-Alexa647 per nucleus of a confluent layer of MCF7 cells to that at 160 ng/ml EGF-Alexa647, where EGFR is saturated with EGF under equilibrium conditions (Hajdu *et al*, 2020). We found that at 20 ng/ml, a concentration at which EGFR phosphorylation was maximal (~92% of that at 160 ng/ml), only ~20% of receptors were bound to EGF with respect to 160 ng/ml (Fig 1E). The phosphorylation level at 20 ng/ml EGF can thus not be explained by transphosphorylation within 2:2 EGF_2-$EGFR_2$ dimers. Instead, the maximal phosphorylation at $\alpha_L = 0.2$ supports a catalytic mechanism that generates phosphorylated EGFR monomers via transient dimer reaction intermediates (Tischer & Bastiaens, 2003; Chung *et al*, 2010).

The EGFR phosphorylation switch at the PM

To relate EGFR phosphorylation to α_L at the PM of live MCF7 cells, EGF-Alexa647 was step-wise increased on MCF7 cells co-transfected with the fluorescent fusion constructs EGFR-mCitrine and PTB-mCherry (phosphotyrosine-binding domain fused to mCherry) that exhibit FRET when PTB-mCherry is bound to phospho-tyrosines on EGFR-mCitrine (pY1086/ pY1148; Offterdinger *et al*, 2004; Baumdick *et al*, 2015; Masip *et al*, 2016; Stanoev *et al*, 2018; Fig EV2A). EGFR-mCitrine expression elevated total EGFR-expression of MCF7 cells by an average factor of ~34 ± 5.5 (mean ± SEM) to that of the related MCF10A cells (~10^5 receptors/cell; Basolo *et al*, 1992; Stanoev *et al*, 2018; Fig 2A). These $2.6 \pm 0.35 \times 10^5$ (mean ± SEM) EGFR-mCitrine expressing MCF7 cells are referred to as EmCit_MCF7. The fraction of phosphorylated EGFR-mCitrine for a given EGF-Alexa647 dose was derived at each pixel from the TCSPC-FLIM (time correlated single photon counting - fluorescence lifetime imaging microscopy) decay profiles of the FRET donor EGFR-mCitrine (Fig EV2B). The pixel-by-pixel fraction of EGFR-mCitrine that exhibits FRET to PTB-mCherry was computed by encoding *a priori* knowledge about the spatial invariance of the excited state lifetime of the EGFR-mCitrine/PTB-mCherry complex (τ_{DA}) and EGFR-mCitrine alone (τ_D) in a global analysis (Verveer *et al*, 2000a, 2000b; Grecco *et al*, 2010; Fig 2B and C). The fraction of phosphorylated EGFR-mCitrine per cell (α_p) was then obtained by averaging the pixel-by-pixel fraction of EGFR-mCitrine that exhibits FRET to PTB-mCherry at the PM as defined by EGF-Alexa647 fluorescence. The corresponding average fraction of EGFR that is bound by EGF (α_L) in the same cell was obtained by normalizing the average ratiometric fluorescence of EGF-Alexa647/EGFR-mCitrine at the PM for each cumulative EGF dose to that at saturating EGF-Alexa647 dose (Reynolds *et al*, 2003; Stanoev *et al*, 2018; Fig 2D). A parametric α_L-α_p plot for each individual cell could thereby be obtained (Fig EV2C). These α_L-α_p dose–response experiments relate receptor phosphorylation response to the fraction of EGFR whose extracellular domain is conformationally activated by EGF. EGF-Alexa647 was increased every 1.5′ to a new cumulative dose. This short time in between EGF administrations relative to the maximal half-time of endocytosis ($t_{1/2}$ ~ 10′, for the highest EGF dose and given EGFR expression of 2.6×10^5 receptors), combined with the vesicular recycling of ligandless EGFR monomers (Baumdick *et al*, 2015) resulted in a net EGFR internalization during the cumulative dose–response experiment that was less than 11 ± 5% for $\alpha_L < 0.4$ at which maximal EGFR phosphorylation is reached, and maximam 19 ± 9% at $\alpha_L = 1$ (Fig 2E, top).

The average α_L-α_p response ($N = 3$, $n = 13$ cells) of EmCit_MCF7 cells that overexpress EGFR-mCitrine by more than two orders of magnitude with respect to endogenous RPTPγ was hyperbolic, with ~50% of EGFR-mCitrine being phosphorylated at ~13% EGF-receptor occupancy (EC50 = 0.10–0.15; Figs 2E, red line and EV2A). This receptor phosphorylation that exceeds EGF-receptor occupancy was similar to that of the endogenous EGFR response (Fig 1E), as was the high level of phosphorylated EGFR-mCitrine ($\alpha_p = 0.63 \pm 0.12$ for $\alpha_L = 0$) in RPTPγ KO EmCit_MCF7 cells (Figs 2E, blue line, 1B and EV2D). Again, similar to WT MCF7 cells (Fig 1A), $p22^{phox}$ KO EmCit_MCF7 cells exhibited a strongly dampened EGFR-mCitrine phosphorylation response ($\alpha_p = 0.28 \pm 0.12$ for $\alpha_L = 1$), substantiating that NOX1-3 activity is necessary for an EGF-induced phosphorylation response (Figs 2E, green line and EV2E). RPTPγ rescue by ectopic expression of RPTPγ-mTFP in RPTPγ KO EmCit_MCF7 cells resulted in EGFR-mCitrine phosphorylation to be reset to low basal levels ($\alpha_p = 0.07 \pm 0.04$ for $\alpha_L = 0$). This rescue shows that high EGFR phosphorylation in RPTPγ KO cells was not an off-target effect of the CRISPR-Cas9 gene editing (Fig 2E, yellow line and C) and substantiates that RPTPγ phosphatase activity suppresses spontaneous EGFR phosphorylation. Furthermore, the phosphorylation response to EGF was restored, now with a switch-like, ultrasensitive instead of a steep hyperbolic response with a defined threshold at 13% receptor occupancy (HC = 2.34; EC50 = 0.13).

To assess how EGFR phosphorylation response is affected by EGFR expression, we compared α_L-α_p response in WT MCF7 ($8 \pm 0.1 \times 10^3$ receptors; mean ± SEM) to that in EmCit_MCF7 ($2.6 \pm 0.35 \times 10^5$ receptors) that express the same level of endogenous RPTPγ. The α_L-α_p response in WT MCF7 cells was reconstructed by relating the average measured α_L in EmCit_MCF7 to the corresponding α_p obtained from western blot analysis of WT MCF7 cells stimulated for 5′ with EGF (0.5–80 ng/ml). α_L is independent of receptor expression level since soluble EGF-Alexa647 was in large excess with respect to the total amount of receptors expressed on the cells (Fig 2D). EGFR phosphorylation was normalized to the maximally attainable phosphorylation after inhibition of PTPs with pervanadate for 5′ (0.33 mM; Baumdick *et al*, 2015). Alike EmCit_MCF7 RPTPγ KO rescue cells, WT MCF7 cells exhibited an ultrasensitive EGFR phosphorylation response with lower α_L threshold (Figs 2F and EV2F, left panel), indicating that the relative RPTPγ/EGFR expression determines the response and not absolute EGFR levels. The ultrasensitive phosphorylation response with low EGF receptor occupancy threshold was also transduced to the early (5′) downstream EGF-dependent activation of Akt and Erk (Fig EV2F, right and middle panels). The corresponding EGF concentration at which this switch occurs (EGFR: 3.7–9.3 ng/ml; Akt: 1.2–3.7 ng/ml; Erk < 1.3 ng/ml) is in the physiological regime between the concentrations found in blood serum (Joh *et al*, 1986; Birk *et al*, 1999; Rich *et al*, 2017) and wound fluid (Sheardown & Cheng, 1996).

In order to relate EGFR phosphorylation response to relative RPTPγ/EGFR expression, we made use of cell-to-cell expression variability in order to relate RPTPγ-mTFP/EGFR-mCitrine expression ratio to the corresponding Hill Coefficient of the α_L-α_p responses in single cells. Hill Coefficients (HC) were obtained by fitting α_L-α_p responses of single EmCit_MCF7 RPTPγ-KO rescue cells to the Hill equation. From the HC versus RPTPγ-mTFP/EGFR-mCitrine fluorescence ratio scatterplot three HC-molecular ratio clusters could be identified, for which the HC and EC50 were determined from the cumulative single cell dose

response data (Fig EV2G). To convert fluorescence into molecular ratios, we normalized background-corrected fluorescence to the background measured in untransfected cells in both fluorescence channels. This normalized fluorescence is directly proportional to the number of fluorescent molecules and is independent on the instrument and settings used, except for excitation and emission wavelength. However, each fluorescent protein has its associated proportionality factor based on its molecular brightness. We transfected a construct in which mTFP in RPTPγ-mTFP was exchanged for mCitrine (RPTPγ-mCitrine) together with EGFR-mCherry to determine the ratio of RPTPγ-mCitrine in these cells over EGFR-mCitrine expressed in EmCit_MCF7 cells (0.4 ± 0.06, mean ± SEM). Using this, the proportionality factor between normalized mTFP and number of mTFP molecules and thus the ratio between EGFR-mCitrine and RPTPγ-mTFP in EmCit RPTPγ

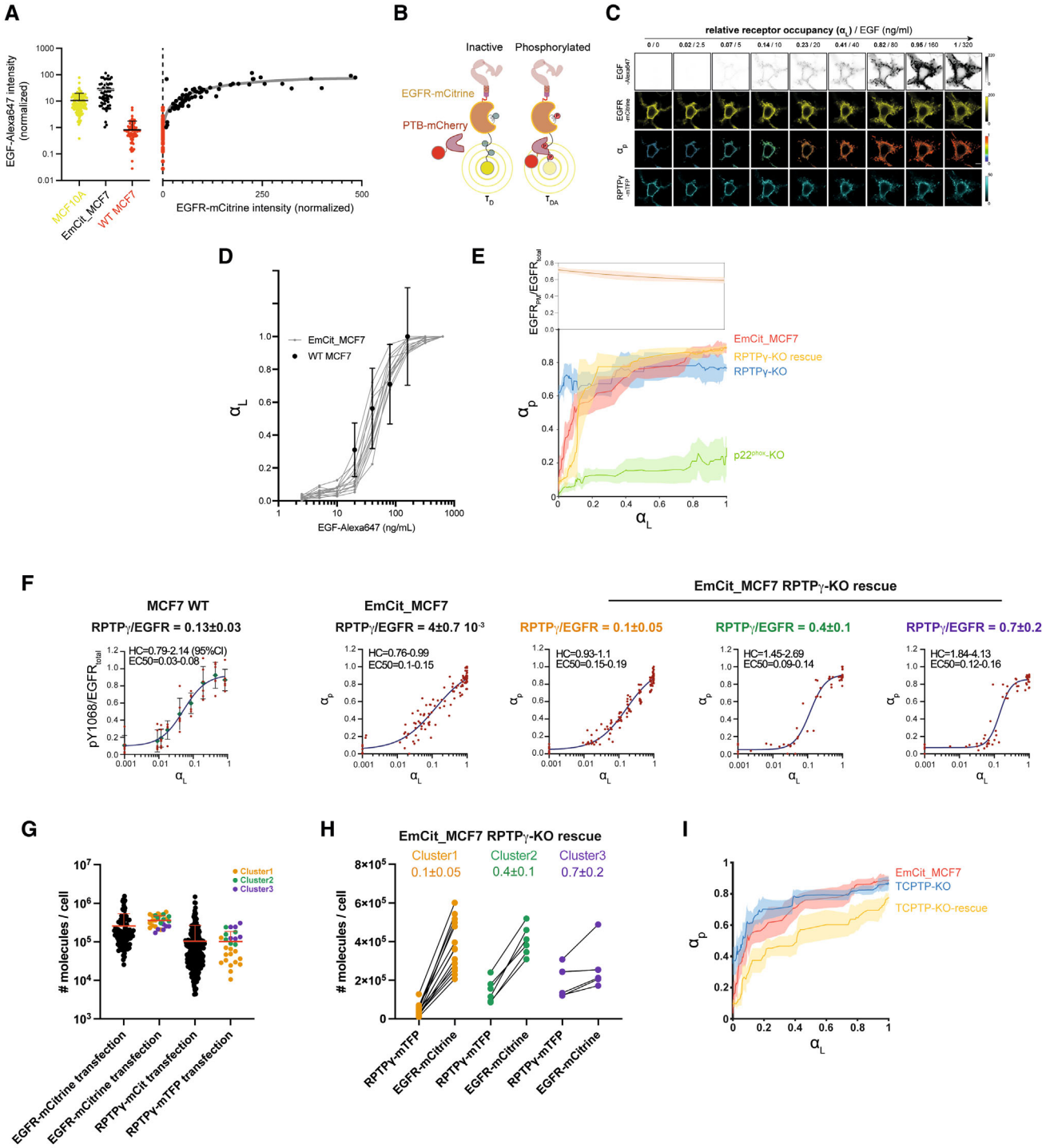

Figure 2.

Figure 2. Ultrasensitive EGFR phosphorylation response is determined by RPTPγ/EGFR stoichiometry and constitutive TCPTP activity.

A Left panel: comparison of normalized EGF-Alexa647 (160 ng/ml; 5′) fluorescence intensity bound to individual endogenous EGFR expressing MCF10A (yellow), to exogenous EGFR-mCitrine expressing EmCit_MCF7 cells (black) and WT MCF7 cells (red); Right panel: normalized EGF-Alexa647 fluorescence plotted against normalized EGFR-mCitrine fluorescence intensity in WT (red) and EmCit_MCF7 (black, with 2nd order polynomal fit: gray line) cells. $N = 3$ biological replicates, $n > 75$ cells, mean ± SD.

B Quantitative imaging of EGFR phosphorylation: Right: Binding of PTB-mCherry (acceptor) to phosphorylated EGFR-mCitrine (donor) causes FRET between donor and acceptor resulting in a reduced excited state lifetime (τ_{DA}) of the donor (mCitrine) in the EGFR-mCitrine/PTB-mCherry complex. Left: Unphosphorylated EGFR-mCitrine exhibits a discrete fluorescence lifetime (τ_D) that is distinct from τ_{DA}. The spatially invariant τ_{DA} and τ_D are shared global parameters for all pixels that enable the mapping of the local fraction of phosphorylated EGFR-mCitrine (α_p, local parameter) within living cells by global analysis.

C Representative fluorescence micrographs of *in cell* EGF-Alexa647 (0–320 ng/ml) dose–response imaging for EGFR phosphorylation in RPTPγ-KO EmCit_MCF7 cells expressing RPTPγ-mTFP. Concentrations of EGF-Alexa647 were increased at 1.5′ time interval and are shown as cumulative dose in ng/mL and corresponding relative receptor occupancies (α_L), obtained by normalizing the ratiometric fluorescence of EGF-Alexa647/EGFR-mCitrine to that at saturating EGF-Alexa647 dose. First row: EGF-Alexa647; Second row: EGFR-mCitrine; Third row: phosphorylated EGFR-mCitrine fraction (α_p); Fourth row: RPTPγ-mTFP; Scale bar: 10 μm.

D Gray: α_L upon each administered dose for individual EmCit_MCF7 cells to cumulative doses of EGF-Alexa647 (2.5–640 ng/ml). $N = 3$ biological replicates, $n = 13$ cells. Black: EGF-Alexa647 bound to WT MCF7 cells at the indicated concentrations normalized to the mean fluorescence intensity at 160 ng/ml EGF-Alexa647 (Fig 1E; mean ± SD, $N = 5$ biological replicates, $n = 16$–19 fields of view).

E Top: Relative fraction of PM-localized fraction of EGFR during the course of *in cell* dose–response experiments in EmCit_MCF7 cells. $N = 3$ biological replicates, $n = 10$ cells. Bottom: EGFR-mCitrine phosphorylation (α_p) plotted as a function of EGF-receptor occupancy (α_L) at the PM to incremental EGF-Alexa647 doses in p22^{phox}-KO (green, $N = 3$ biological replicates, $n = 12$ cells), RPTPγ-KO (blue, $N = 3$ biological replicates, $n = 14$ cells), RPTPγ-KO with RPTPγ-mTFP ectopic expression (yellow, $N = 4$ biological replicates, $n = 13$ cells) and WT (red, $N = 3$ biological replicates, $n = 13$ cells) EmCit_MCF7 cells. Solid lines: moving medians from single cell profiles; shaded bounds: median absolute deviations.

F Left: EGFR- (pY1068-) phosphorylation response in WT MCF7 cells obtained from western blots normalized to maximal phosphorylation obtained by inhibiting all phosphatases by 0.33 mM pervanadate ($N = 6$; red symbols with mean ± SD and fit to the hill equation (solid line)) at 0 (plotted as 0.001 to fit the logarithmic *x*-axis), 0.5, 1, 2, 5, 10, 20, 40, and 80 ng/ml plotted against corresponding α_L (obtained from *in cell* dose response experiments in EmCit_MCF7 cells (D)). Correspondig molecular RPTPγ/EGFR-ratio (see G, H, Fig EV2H) is depicted above the graphs; Inserted into each graph are the values of Hill coefficient (HC) and EC50 of the fitted hill equation (95% confidence interval). 2nd graph: Same as left graph with α_p plotted vs α_L both obtained from *in cell* dose response experiments in EmCit_MCF7 cells. 3rd–5th graph: Same as 2nd graph for EmCit_MCF7 RPTPγ-KO with RPTPγ-mTFP ectopic expression clustered by RPTPγ/EGFR-expression ratio and HC (Fig EV2G).

G Number of molecules obtained by normalizing background-subtracted fluorescence intensities of individual transfected cells against the mean background intensity of untransfected cells, yielding relative expressions levels independent on the fluorophore (Materials and Methods). This value was then set into proportion to the known mean number of EGFR per MCF10A cell to yield absolute molecule count/cell. 1st column: EGFR-mCitrine in EmCit_MCF7 cells ($N = 3$ biological replicates, $n = 102$ cells); 2nd column EGFR-mCitrine expressed in EmCit_MCF7 RPTPγ-KO expressing RPTPγ-mTFP ($N = 3$ biological replicates, $n = 26$ cells); 3rd column: RPTPγ-mCitrine in MCF7 cells expressing additionally EGFR-mCherry ($N = 3$ biological replicates, $n = 253$ cells); 4th column: RPTPγ-mTFP expressed in EmCit_MCF7 RPTPγ-KO ($N = 3$ biological replicates, $n = 26$ cells; individual cells with mean + SD). Color code in 2nd and 4th column is attribution to respective cluster (H and Fig EV2G).

H Number of RPTPγ-mTFP and EGFR-mCitrine molecules in EmCit_MCF7 RPTPγ-KO expressing RPTPγ-mTFP plotted for the three HC-RPTPγ/EGFR-ratio clusters identified in Fig EV2G together with RPTPγ over EGFR molecular ratio (top; mean ± SD).

I EGFR-mCitrine phosphorylation (α_p) plotted as a function of EGF-receptor occupancy (α_L) at the PM to incremental EGF-Alexa647 doses in WT (red, $N = 3$ biological replicates, $n = 13$ cells), TCPTP-KO (blue, $N = 3$ biological replicates, $n = 14$ cells) and TCPTP-KO with TCPTP-mTFP ectopic expression (yellow, $N = 3$ biological replicates, $n = 13$ cells) EmCit_MCF7 cells. Solid lines: moving medians from single cell profiles; shaded bounds: median absolute deviations.

Source data are available online for this figure.

KO rescue cells were determined (see Materials and Methods). While the molecular numbers can also be calculated using the previously known number of EGFR per MCF10A cells as reference point, the fluorescence background normalization procedure alone yields RPTPγ-mTFP/EGFR-mCitrine molecular ratios that are independent of absolute molecular numbers. This procedure was validated by the very similar molecular distributions obtained for RPTPγ-mCitrine and RPTPγ-mTFP transfections (Fig 2G) and yielded an average RPTPγ/EGFR molecular ratio of 0.1 ± 0.05, 0.4 ± 0.1 and 0.7 ± 0.2 for the three clusters (mean ± SD; Fig 2F and H). Using the ratio of RPTPγ-mCitrine stably expressed in MCF7 cells to endogenous RPTPγ obtained by western blot (100 ± 15; mean ± SEM, $N = 3$, $n = 7$, Fig EV2H), we could also estimate that WT MCF7 cells express $1 \pm 0.2 \times 10^3$ RPTPγ/cell corresponding to 13 ± 3% of endogenous EGFR expression ($8 \pm 1 \times 10^3$/cell; mean ± SEM).

Going from endogenous RPTPγ in EmCit_MCF7 cells (RPTPγ/EGFR-mCitrine = $4 \pm 0.7 \times 10^{-3}$) to the cluster with highest (0.7 ± 0.2) RPTPγ-mTFP/EGFR-mCitrine expression ratio in Em_Cit RPTPγ KO rescue cells, a clear progression from hyperbolic to ultrasensitive switch-like EGFR-mCitrine α_L-α_p response was apparent (Fig 2F). This correlation between RPTPγ/EGFR ratio and ultrasensitivity of the phosphorylation response corroborates that qualitative phosphorylation response properties are determined by the relative expression of RPTPγ over EGFR and emerge from EGFR-RPTPγ interaction dynamics. Because at the highest RPTPγ-mTFP/EGFR-mCitrine ratio RPTPγ-mTFP dephosphorylating activity is dominant with respect to other PTPs, the ultrasensitive response indicated a dynamical signature of a mutual inhibition motif (toggle switch) between EGFR and RPTPγ.

The hyperbolic phosphorylation response at RPTPγ-mTFP/EGFR-mCitrine ratios below 0.1, however, indicated that other PTPs modulated the response dynamics of the RPTPγ/EGFR toggle switch. We, therefore, investigated whether another EGFR PTP, TCPTP (*PTPN2*), had an effect on the phosphorylation response dynamics of the RPTPγ/EGFR system. Knock-out of this ER-associated PTP (Fig EV2I) resulted in a clear increase in basal EGFR-mCitrine phosphorylation ($\alpha_p = 0.35 \pm 0.13$ for $\alpha_L = 0$) in EmCit_MCF7 cells, while maintaining a relatively steep residual phosphorylation response to EGF (EC50 = 0.19 (0.11–0.33); Hill Coeff = 1.01 (0.71–1.91); Figs 2I, blue line and EV2J). Ectopic expression rescue of TCPTP-mTFP in these KO-cells restored the low basal EGFR phosphorylation ($\alpha_p = 0.09 \pm 0.08$ for $\alpha_L = 0$), showing that TCPTP activity plays a role in maintaining a low basal EGFR phosphorylation level in the absence of growth factor stimuli. However, this rescue also resulted in a more gradual hyperbolic phosphorylation response (EC50 = 0.41 (0.26–0.48); Hill Coeff = 0.93 (0.8–1.24); Figs 2I, yellow line and EV2K), indicating a constitutive suppressive

dephosphorylation activity that dampens the ultrasensitive EGFR phosphorylation response.

The EGF-induced RPTPγ oxidation switch at the PM

To experimentally assess whether RPTPγ catalytic cysteine oxidation to cysteine sulfenic acid by NOX-generated H_2O_2 (Bae *et al*, 1997; Denu & Tanner, 1998; Meng *et al*, 2002; Reynolds *et al*, 2003) constitutes an inhibitory link from EGFR to RPTPγ, we developed a live cell assay to measure the fraction of oxidized RPTPγ (α_{ox}) as function of receptor EGF-occupancy (α_L; Fig 3A and B). For this, the dimedone warhead derived DYn2 (Paulsen *et al*, 2012) was coupled to Atto590-azide by Cu-based click chemistry (Rostovtsev *et al*, 2002) to obtain a cell permeable mCitrine-FRET acceptor probe DyTo that specifically binds to the sulfenic acid form of oxidized cysteines (Appendix Fig S1A). To image RPTPγ catalytic cysteine oxidation, MCF7 cells ectopically expressing RPTPγ-mCitrine and EGFR-mTFP (EmTFP_MCF7, $2.6 \pm 0.35 \times 10^5$ receptors/cell, Fig 2A) were stimulated with different doses of EGF for 5′, followed by 5′ incubation with DyTo (Fig 3C and Appendix Fig S1B). TCSPC FRET-FLIM of the donor mCitrine was used to specifically map the fraction of RPTPγ-mCitrine that is in molecular proximity and thus bound to DyTo (α_{ox}). By encoding *a priori* knowledge about the spatial invariance of the excited state lifetime of the RPTPγ-mCitrine bound by DyTo (τ_{DA}) and RPTPγ-mCitrine alone (τ_D) in a global analysis, α_{ox} could be determined in each pixel exhibiting RPTPγ-mCitrine fluorescence. Treatment with 8 mM H_2O_2, as positive control for the assay, resulted in a pronounced average fraction of RPTPγ-mCitrine that exhibited FRET to DyTo throughout the cells ($\alpha_{ox} = 0.86 \pm 0.07$; Fig 3C, right panel). Specificity of the assay was apparent from the fact that H_2O_2 treated EmTFP_MCF7 cells expressing RPTPγ^{C1060S}–mCitrine mutant where the catalytic cysteine has been replaced by serine, exhibited average α_{ox} values close to zero (negative control; $\alpha_{ox} = 0.07 \pm 0.04$). Donor-based mCitrine-DyTo FRET-FLIM molecular proximity imaging (Bastiaens & Squire, 1999; Grecco *et al*, 2011), thus, specifically detects the oxidation of the catalytic cysteine of RPTPγ, despite DyTo binding to all oxidized cysteines on proteins (Fig 3C and Appendix Fig S1B). To obtain spatial information about where RPTPγ is oxidized, we morphologically distinguished the PM appearing as elongated continuous structures (like the serpentine structures of ruffles) from endosomal vesicles that appear as distinct round objects within the boundaries of the PM structures.

Imaging α_{ox} as function of EGF dose (5–160 ng/ml; Fig 3C, right panel) showed a similar switch-like response for RPTPγ catalytic cysteine oxidation at the PM as observed for EGFR phosphorylation in EmCit_MCF7 RPTPγ KO rescue cells (Fig 2E, yellow line). In these RPTPγ-mCitrine expressing EmTFP_MCF7 cells, RPTPγ-mCitrine oxidation also switched below a ~20% EGF-receptor occupancy (~20 ng/ml EGF-Alexa647) from a ~10% basal level to ~60% RPTPγ-mCitrine oxidation (Fig 3C, orange symbols). This EGFR-activity-coupled oxidative impairment of RPTPγ catalytic activity occurred at the PM, whereas RPTPγ-mCitrine was in its enzymatically active, reduced catalytic cysteine state in endocytic structures (Fig 3C, blue symbols). This indicates that EGF-induced catalytic cysteine oxidation to sulfenic acid was mostly restricted to RPTPγ-mCitrine on the PM. Consistent with the dampened phosphorylation response (Fig 2E, green line), p22^{phox}-KO EmTFP_MCF7 cells exhibited no RPTPγ-mCitrine oxidation response to increasing EGF doses, whereas 8 mM H_2O_2 treatment resulted in full RPTPγ-mCitrine oxidation on the PM as well as in endocytic structures (Fig 3D).

We similarly assessed catalytic cysteine oxidation of ER-associated TCPTP in EmTFP_MCF7 cells that ectopically express TCPTP-mCitrine. Imaging TCPTP-mCitrine oxidation as function of EGF dose (5–160 ng/ml) showed a basal (~30%) and spatially even oxidation along the ER reticular structures independent of EGF stimulus. Only at the highest doses of EGF (160 ng/ml) a slight but significant oxidation increase in the PM-proximal pool (Liou *et al*, 2005; Haj *et al*, 2012) of ER-associated TCPTP-mCitrine could be detected (Fig 3E). This indicates that the EGF-induced H_2O_2 gradient that is produced by PM associated NOX1-3 activity is confined to the immediate vicinity of the PM, likely due to the highly reducing environment of the cytoplasm that contains antioxidant systems like peroxiredoxin-thioredoxin (Rhee, 1999; Rhee *et al*, 2005; Woo *et al*, 2010). On the other hand, the overall low but significant level of TCPTP-mCitrine catalytic cysteine oxidation throughout the ER indicates constitutive ER-associated NOX activity (Jagnandan *et al*, 2007). These results show that TCPTP maintains its constitutive dephosphorylating activity on EGFR during growth factor stimulation, exhibiting a low level of oxidation that is largely uncoupled from EGF-induced EGFR activity. The EGF-induced steep H_2O_2 gradient that emanates from the PM, thus, constrains catalytic cysteine oxidation mostly to the pool of RPTPγ at the PM.

Recycling RPTPγ-EGFR generates a growth factor responsive spatial redox cycle

We next investigated whether differential vesicular trafficking of EGFR and RPTPγ has a function for redox-dependent EGF sensing and signaling at the PM. We first measured the intracellular redistribution over time of ectopically expressed RPTPγ-mCitrine and EGFR-mCherry in EE, recycling (RE) and LE compartments after a receptor saturating EGF stimulus (160 ng/ml). Endosomal compartments were immunostained against markers for early-(EEA1), recycling-(Rab11a) and LEs (Rab7) after 0′, 15′, 30′ and 60’ EGF stimulus and fixation of cells. Prior to EGF stimulus, RPTPγ-mCitrine and EGFR-mCherry exhibited significant co-localization on the PM as well as endosomal structures containing Rab11 (Fig 4A, top panel and B, left panels), indicating constitutive vesicular recycling of both proteins. After receptor saturating (160 ng/ml) EGF stimulus, RPTPγ remained at the PM and RE (Fig 4A, bottom panel and B, left panels), whereas EGFR separated from RPTPγ, trafficking towards the LE via the EE (Figs 4B, and EV3A and B). This is consistent with constitutive recycling of EGFR being disrupted upon the generation of EGF-induced EGFR complexes that unidirectionally traffic from the PM, via EEs to the LE (Baumdick *et al*, 2015), whereas vesicular recycling of RPTPγ continued. In contrast to RPTPγ-mCitrine expressing MCF7 cells, only a small fraction of EGFR-mCitrine was depleted from the PM upon receptor saturating EGF stimulation in RPTPγ-KO cells. These did not reach the LE, possibly due to vesicular recycling as apparent from co-localization with EEs and REs (Fig 4B, dotted profiles). The altered EGFR-trafficking upon RPTPγ-KO, thus, maintains a substantial fraction of active, phosphorylated EGFR on the PM, irrespective of EGF

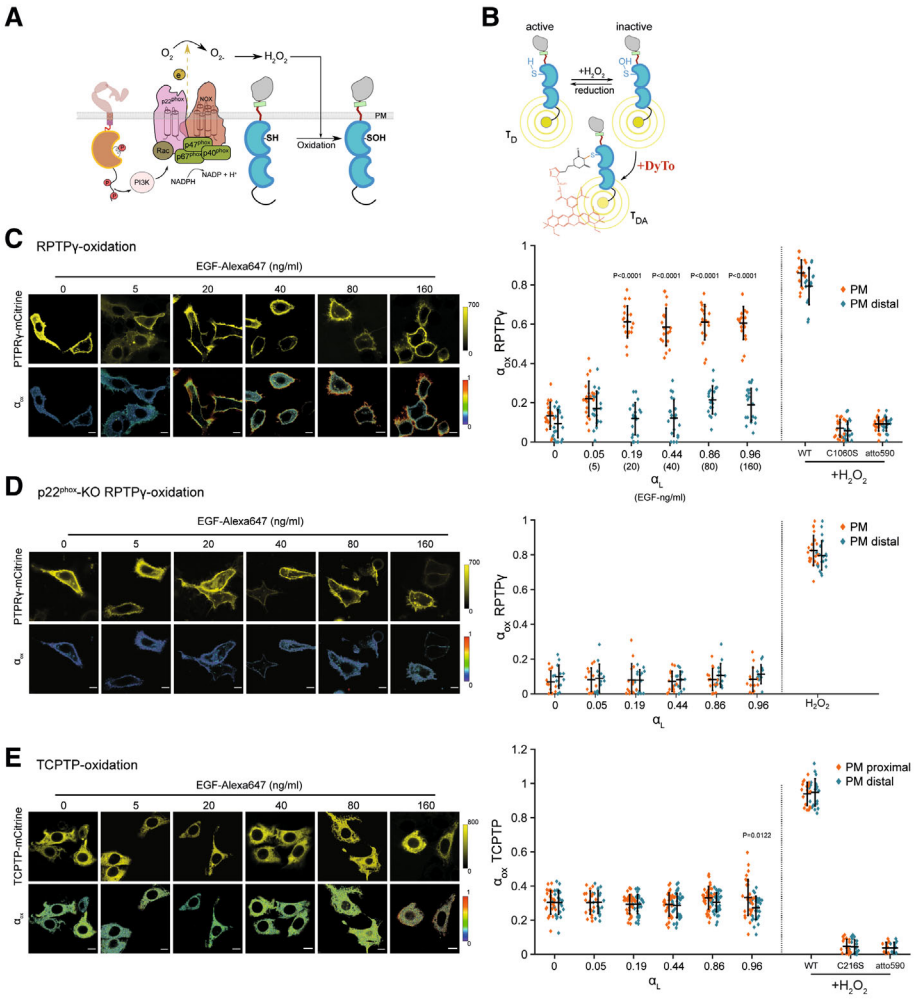

Figure 3. EGF-dependent ROS-generation couples EGFR-phosphorylation to RPTPγ oxidation.

A Reaction schematic of EGFR-dependent PTP-oxidation: Phosphorylated EGFR (red circles) activates PI3K, which results in the activation of Rac-GTPase and the cytosolic components of NOX-assembly like p40^{phox}, p47^{phox} and p67^{phox}. Recruitment of these components to the PM-based major NOX-unit and p22^{phox} subunit, mediates the transfer of electrons from the cytosolic NADPH to extracellular oxygen (O_2) leading to the formation of superoxide anion (O_2^-) that dismutates to hydrogen peroxide (H_2O_2). Diffusion of H_2O_2 through the PM causes the cysteine oxidation of the PM-vicinal PTPs, from thiol (SH) to sulfenic acid (SOH) state.

B Schematic of FLIM assay for the quantitative imaging of PTP-oxidation in live cells: Binding of DyTo (atto590, acceptor) to oxidized cysteines (S-OH) of PTP-mCitrine (donor) results in FRET between donor and acceptor reducing the excited state lifetime of the donor (τ_{DA}). Spatial invariance of τ_{DA} and τ_D enable the mapping of the fraction of oxidized PTP-mCitrine (α_{ox}, local parameter) by global analysis.

C–E (C) *In cell* EGF-dose response imaging for RPTPγ-mCitrine oxidation. Left panel: Representative confocal micrographs of RPTPγ-mCitrine in EmTFP_MCF7 cells (top row) together with its oxidized fraction estimated using DyTo-FLIM (α_{ox}, bottom row), upon 10′ stimulation with EGF-Alexa647 (0–160 ng/ml) including 5′ together with 0.5 mM DyTo. Scale bar: 10 μm. Right panel: Quantification depicting the PM-proximal (orange) and PM-distal (blue) oxidized fractions as functions of receptor occupancy (α_L) and corresponding EGF-Alexa647, or H_2O_2 concentration in EmTFP MCF7 cells expressing RPTPγ-mCitrine (WT) or RPTPγ^{C1060S}-mCitrine (C1060S) as well as WT cells treated with 0.5 mM atto590 instead of DyTo (atto590). Mean of individual cells (symbols) with mean ± SD (black lines), $N = 3$ biological replicates, $n = 13$–15 cells per EGF dose. P: unpaired two-tailed *t*-test, between PM (serpentine peripheral structures) and endosomal (vesicular structures) fractions. (D) Same as in (C), for RPTPγ-mCitrine oxidation in p22^{phox}-KO cells. $N = 3$ biological replicates, $n = 14$–26 cells per EGF dose. (E) Same as in (C), for TCPTP-mCitrine or TCPTP^{C216S}-mCitrine (C216S) oxidation in EmTFP_MCF7 cells. $N = 3$ biological replicates, $n = 18$–21 cells per EGF dose.

stimulus, hindering efficient lysosomal degradation of liganded EGFR complexes. Furthermore, deregulated post-translational EGFR trafficking in RPTPγ-KO cells was also apparent from substantial colocalization of EGFR with the ER (Fig EV3C) and other endomembrane structures as well as strong enrichment on PM ruffles. This shows that EGFR trafficking to the PM after its biosynthesis and ER-insertion as well as its vesicular dynamics is deregulated in the absence of RPTPγ, indicating a strong functional coupling between EGFR and RPTPγ.

In order to investigate whether RPTPγ is dynamically maintained at steady-state at the PM by Rab11-activity-driven vesicular recycling, we enhanced the biogenesis of RE structures by ectopic BFP-Rab11a expression (Fig 4C). This caused the distribution of RPTPγ-mCitrine to be rebalanced towards large perinuclear BFP-Rab11

positive endocytic structures in dependence on the level of BFP-Rab11a expression. Continuous vesicular recycling that sustains RPTPγ at the PM was apparent from the time-dependent equilibration of photoactivated paGFP-RPTPγ at the PM after photoactivation on BFP-Rab11-positive RE or mCherry-RPTPγ-positive endosomal structures (Figs 4D, and EV3D and E). The fraction of photoactivated paGFP-RPTPγ at the PM was thereby strongly dependent on BFP-Rab11 expression. RPTPγ levels at the PM are, thus, dynamically maintained at steady-state by Rab11-activity-mediated vesicular recycling.

To investigate if the change in trafficking upon receptor saturating EGF stimulus is reflected in the nanoscale organization of EGFR and RPTPγ, super resolution radial fluctuation microscopy of Alexa647-SNAP-EGFR and RPTPγ-mCitrine stably expressed in MCF7 cells was applied after ultra-rapid cryo-arrest on a microscope (Huebinger *et al*, 2021). This showed a co-organization of Alexa647-SNAP-EGFR nanoclusters within larger RPTPγ-mCitrine patches along the PM in serum-starved cells (Fig 4E). However, after 15′ 100 ng/ml EGF stimulus, EGFR clusters were segregated from RPTPγ at the PM as well as in endocytic structures. This change in EGFR-RPTPγ nanoscale organization upon close-to-receptor-saturating EGF stimulus indicates an interaction between EGFR and RPTPγ at the PM that is disrupted upon formation of EGF-EGFR at receptor-saturating EGF doses.

We, therefore, examined whether a constitutive interaction of RPTPγ with EGFR monomers exists that is disrupted upon the generation of liganded EGFR. For this, we carried out immunoprecipitation of RPTPγ-mCitrine and measured the extent of EGFR pull-down as function of EGF concentration in MCF7 cells co-transfected with EGFR and RPTPγ-mCitrine (Fig 4F). An interaction between EGFR and RPTPγ-mCitrine was apparent in the absence of stimulus as well as at doses of EGF (5 and 20 ng/ml) that occupied a low percentage of available receptors (5 ± 2 and 19 ± 4%, respectively; Fig 2D). Under these conditions, phosphorylated EGFR monomers predominate at the PM (Fig 1D and E), indicating that RPTPγ constitutively interacts with EGFR monomers. However, this interaction did not occur upon treatment for 5′ with EGF doses that saturate EGFR binding sites (160 and 320 ng/ml), indicating that RPTPγ does not interact with liganded receptors. Neither catalytic cysteine to serine mutation (RPTPγ^{C1060S}-mCitrine) nor catalytic cysteine oxidation by 8 mM H_2O_2 affected the amount of co-immunoprecipitated EGFR, showing that the oxidation state of RPTPγ does not affect its constitutive interaction with ligandless EGFR.

To next relate EGF dependent RPTPγ-EGFR vesicular trafficking to RPTPγ inactivation dynamics, we compared temporal profiles of catalytic cysteine oxidation for a receptor-saturating (160 ng/ml) EGF-Alexa647 stimulus to a receptor sub-saturating (α_L = 19 ± 4%, Fig 2D) but strongly EGFR-phosphorylating (Fig 2E) stimulus (20 ng/ml). At both EGF concentrations, RPTPγ attained the maximally oxidized, inactive state at the PM within the timescale of maximal EGFR-phosphorylation (~10′; Figs 4G and EV3F–H). However, whereas the 160 ng/ml sustained EGF-stimulus caused RPTPγ oxidation to fall back to basal levels in ~20′ (Fig 4G, green), the 20 ng/ml sustained EGF-stimulus caused the dynamic equilibration to a high steady-state oxidation level (Fig 4G, magenta). In order to relate these RPTPγ oxidation profiles for different EGF concentrations to RPTPγ-EGFR trafficking dynamics, we obtained high-resolution radial spatial–temporal maps (STMs; Stallaert *et al*, 2018; Stanoev *et al*, 2018) of EGFR-mCherry/RPTPγ-mCitrine from 2-h CLSM (confocal laser scanning microscopy) time-lapse imaging (Fig 4H and I). These STMs confirmed that a receptor-saturating (160 ng/ml) EGF stimulus rapidly depleted EGFR, while RPTPγ density at the PM increased over time (Fig 4H). This causes levels of phosphorylated EGF-EGFR at the PM to drop to a level that cannot sustain the necessary activity of NOX1-3 enzymes. In contrast, the continuous generation and internalization of only a small fraction of liganded EGF-EGFR upon a receptor sub-saturating (20 ng/ml) EGF stimulus removes only a small fraction of EGFR from the PM. Afterwards, a steady-state of relatively high fraction of EGFR is dynamically maintained by recycling EGFR monomers (Fig 4I). In this steady-state, re-phosphorylation of recycled EGFR-monomers at the PM sustains Nox1-3 activity, which in turn re-oxidize and inactivate recycled RPTPγ (Fig 4G and I), enabling prolonged signaling of monomeric EGFRp at low EGF levels.

Autocatalytic RPTPγ-EGFR-TCPTP toggle switch dynamics

To investigate how EGFR phosphorylation responses at low-receptor occupancy arise from PTP-EGFR reactions at the PM, the experimentally obtained α_L-α_p responses (Fig 2E, F and I) were globally fitted to a RPTPγ-EGFR-TCPTP autocatalytic toggle switch network model that reaches steady state (Fig 5A and B). The three ordinary differential equations (ODEs) in Fig 5B describe the dynamics of the symmetric autocatalytic toggle switch reaction scheme with all the possible causal links depicted in Fig 5A. The ODEs have been normalized (λ_{EE} = EGFR$_T$, λ_p = k1) to obtain reactant fractions (EGF-EGFRp/EGFR$_T$, EGFRp/EGFR$_T$, RPTPγ$_A$/RPTPγ$_T$), yielding comparable parameters that describe maximal rate of dephosphorylation by RPTPγ ($\Gamma_{1,3} = \gamma_{1,3}$. RPTPγ$_T$/EGFR$_T$) or constant rate of dephosphorylation by TCPTP ($\Gamma_{2,4} = \gamma_{2,4}$.TCPTP/EGFR$_T$) of ligandless EGFRp ($\Gamma_1$, Γ_2) or liganded EGF-EGFRp (Γ_3, Γ_4), as well as the maximal rate of oxidative RPTPγ inhibition over reactivation (B = β EGFR$_T$/k1). The catalytic (second-order rate constants: ε1–ε4) and autocatalytic (second-order rate constants: α1–α4) EGFR phosphorylation reactions are based on evidence that extracellular domain symmetric (EGFR$_2$, EGF$_2$-EGFR$_2$: ExSym), and asymmetric (EGF-EGFR$_2$: ExAsym) dimers are transient ($t_{1/2}$ ~ 1–10 s) reaction intermediates (Chung *et al*, 2010; Low-Nam *et al*, 2011; Salazar-Cavazos *et al*, 2020) that (auto-)catalytically generate phosphorylated ligandless (EGFRp) and liganded (EGF-EGFRp) monomers (Fig EV5A; Verveer *et al*, 2000b; Reynolds *et al*, 2003; Ichinose *et al*, 2004; Stanoev *et al*, 2018). Physical invariant parameters were linked among the responses of the four expression perturbations groups (RPTPγ, TCPTP, p22^{Phox}, and EGFR) during iterative parameter estimation at steady state (d**EGFR**$_{p/T}$/dt = d**EGF-EGFR**$_{p/T}$/dt = d**RPTPγ**$_{A/T}$/dt = 0), improving model testing and definition of error space (Beechem, 1992; Materials and Methods). The goodness of fit to the multi-dimensional α_L-α_p data surface is shown in Fig EV4C, and the obtained parameters as well as their linkage among expression perturbation experiments are listed in Fig EV4B.

Catalysis (ε_i, i = 1,4) occurs when unliganded (ε_1), or liganded ExSym (ε_4) as well as ExAsym ($\varepsilon_{2,3}$) unphosphorylated dimers generate liganded (EGF-EGFRp) or unliganded (EGFRp) phosphorylated monomers. Autocatalysis (α_i, i = 1–4) occurs when EGFRp or EGF-EGFRp monomers generate more EGFRp or EGF-EGFRp via ligandless (α_1) or liganded ExSym (α_4) dimers as well as ExAsym ($\alpha_{2,3}$) dimers (Fig EV4A). The expression invariant second-order rate

constants of catalysis (ε_1–ε_4) and autocatalysis (α_1–α_4) were linked among the fits of all α_L-α_p responses (Fig EV4B). Comparison of the catalysis rate constants shows the expected efficient catalytic EGFR phosphorylation via ExSym (EGF_2-$EGFR_2$) dimers, whereas catalysis via ExAsym dimers (EGF-$EGFR_2$) is an order of magnitude less efficient and via unliganded ($EGFR_2$) dimers three orders of magnitude

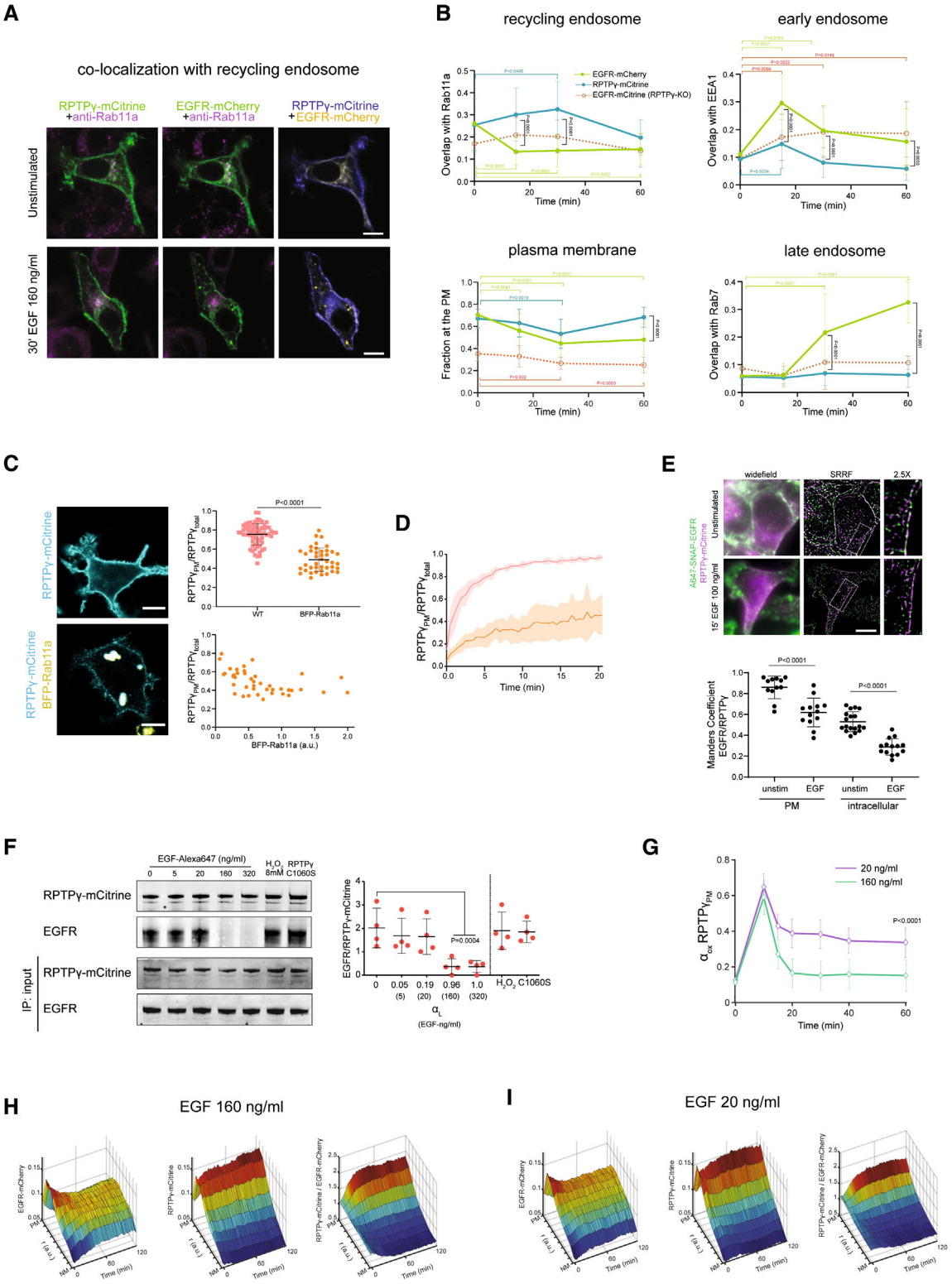

Figure 4.

Figure 4. EGFR-RPTPγ redox-phosphorylation-cycles are dynamically coupled through space.

A Representative confocal micrographs of MCF7 WT cells showing the co-localization of RPTPγ-mCitrine (1st column: green; 3rd column: blue) and EGFR-mCherry (2nd column: green; 3rd column: yellow) with recycling-endosome defined by immunostaining against Rab11a (magenta), without (top row) or after 30′ EGF-DyLight405 stimulus (160 ng/ml; bottom row). Scale bar: 10 μm.

B Fraction of RPTPγ-mCitrine (cyan) or EGFR-mCherry (green) that spatially overlaps with Rab11a (top left, $N = 3$, $n = 23$–26 cells per timepoint), PM (bottom left, $N = 3$ biological replicates, $n = 15$–17 cells), EEA1-positive EEs (top right, $N = 3$ biological replicates, $n = 25$–28 cells) or Rab7-positive LEs (bottom right, $N = 3$ biological replicates, $n = 23$–27 cells) in MCF7 cells as function of time after 160 ng/ml EGF-stimulus. Orange symbols/dotted line: same for EGFR-mCitrine in RPTPγ-KO cells ($N = 3$ biological replicates, $n = 17$–21 cells). P: unpaired two-tailed *t*-test; colored *P* values compare to the respective species before stimulation, black in between species.

C Left: Representative confocal micrographs of MCF7 cells depicting the steady state localization of expressed RPTPγ-mCitrine (cyan), without (top) or with co-expression of BFP-Rab11a (yellow, bottom). Top right: Quantification of PM-localized fraction of RPTPγ-mCitrine without (WT) and with co-expression of BFP-Rab11a. Bottom right: Fraction of RPTPγ-mCitrine localized to the PM in individual cells as a function of BFP-Rab11a expression level, measured by mean BFP-fluorescence intensity. Scale bar: 10 μm. $N = 2$ biological replicates, $n > 40$ per condition, mean ± SD; *P*: unpaired two-tailed *t*-test.

D Fraction of fluorescent paGFP-RPTPγ at the PM over time after photoactivation of paGFP exclusively in the perinuclear region, in cells with (orange) or without (pink) co-expression of BFP-Rab11a. mean ± SD, $N = 3$ biological replicates, $n = 4$–7 cells.

E Upper panel: Dual-color widefield images (1st column), SRRF reconstructions (2nd column) with magnifications of boxed areas (3rd column) of Alexa647-SNAP-EGFR (green) and RPTPγ-mCitrine (magenta) of cryo-arrested MCF7 cells, unstimulated (top row) or stimulated with 100 ng/ml EGF (bottom row) for 15′. Scale bar: 10 μm. Lower panel: corresponding Manders colocalization coefficients for Alexa647-Snap-EGFR/RPTPγ-mCitrine from SRRF reconstructions on intracellular compartments or PM area for unstimulated ($n = 12$–18) and 15′ EGF-stimulated ($n = 13$–14) cells. mean ± SD, *P*: unpaired two-tailed *t*-test.

F Left: Representative IP-western blot showing co-IP of EGFR (2nd row) upon RPTPγ-mCitrine (1st row: lanes 1–6) or RPTPγ^{C1060S}-mCitrine (lane 7) pull-down by anti-GFP antibody from lysates of MCF7 cells co-transfected with EGFR and RPTPγ-mCitrine or RPTPγ^{C1060S}-mCitrine: without stimulus (0 ng/ml), upon 10′ stimulus with EGF-Alexa647 (5–320 ng/ml, also displayed as corresponding receptor-occupancy α_L, Fig 2D) or 8 mM of H_2O_2. 3rd and 4th row: total protein concentrations of RPTPγ-mCitrine and EGFR in the lysate measured by western blot as input control for the Co-IP. Right: corresponding ratiometric quantification of co-immunoprecipitated EGFR over pulled down RPTPγ-mCitrine or RPTPγ^{C1060S}-mCitrine protein bands (mean ± SD, $N = 4$ biological replicates, *P*: unpaired two-tailed *t*-test).

G Oxidized fraction of RPTPγ-mCitrine (α_{ox}) at the PM of live EmTFP_MCF7 cells estimated using DyTo-FLIM at indicated timepoints upon receptor sub-saturating (20 ng/ml, magenta, $N = 3$ biological replicates, $n = 21$–25 cells) or saturating (160 ng/ml, green, $N = 3$ biological replicates, $n = 23$–26 cells) sustained EGF-Alexa647 stimulus. mean ± SD, *P*: unpaired two-tailed *t*-test between 20 ng/ml and 160 ng/ml treatment ($P < 0.001$ from 15′ to 60′).

H, I (H) Average spatial–temporal maps constructed from confocal micrographs obtained at 1′ interval from live MCF7 cells showing the distributions of EGFR-mCherry (left), RPTPγ-mCitrine (middle) and RPTPγ-mCitrine/EGFR-mCherry (right) as a function of their normalized and binned radial distance (r) between PM and nuclear membranes (NM) and time (0–120′), upon sustained treatment with receptor-saturatig ($\alpha_L = 0.96 \pm 0.05$) dose of 160 ng/ml EGF-Alexa647. $N = 3$ biological replicates, $n = 14$ cells. (I) Same as (H) for a receptor-subsaturating ($\alpha_L = 0.19 \pm 0.04$) dose of 20 ng/ml EGF-Alexa647. $N = 3$ biological replicates, $n = 13$ cells.

less efficient. However, when unliganded EGFR is phosphorylated, it increases kinase activity for unphosphorylated ligandless EGFR by three orders of magnitude (compare ε1 to α1, Fig 3C), to a similar level as that in the catalysis through liganded ExSym dimers. Also kinase activity in the ExAsym dimer reactions was increased to a similar level by phosphorylation of EGFRp or EGF-EGFRp (Fig 5C). This is consistent with regulatory tyrosine phosphorylation, such as pY845 (Sato *et al*, 1995), causing a conformational change on intracellular kinase domains that enhances EGFR dimerization as well as its intrinsic kinase activity (Shan *et al*, 2012; Baumdick *et al*, 2018). In order to determine the relative contribution of the four catalytic and four autocatalytic reactions to the steady state EGFR phosphorylation (EGF-EGFRp + EGFRp) for a given α_L, we multiplied the kinetic rate constants (ε_1–ε_4, α_1–α_4) with the computed abundances of the reaction substrates (EGFR, EGFRp, EGF-EGFR, EGF-EGFRp) that form the eight possible transient EGFR dimeric reaction intermediates (Fig EV4A). This showed that the autocatalytic reaction by ligandless EGFRp-EGFR dimer transients, associated with the rate constant α_1, dominates the EGFR phosphorylation reaction in the physiological EGF receptor occupancy range ($\alpha_L = 0.01$–0.1; Fig 5D), where the major phosphorylated reaction product is EGFRp (Fig EV4D). However, in order to initiate this autocatalytic reaction, the much less abundant catalytic ExAsym (ε2) reaction has to generate EGFRp, whereas the remaining catalytic ExAsym (ε3) and ExSym (ε4) reaction generate EGF-EGFRp and, therefore, can only trigger the ligandless autocatalytic reaction (α1) via ExAsym autocatalysis (α2; Fig 5D, inset). The autocatalytic reaction by ligandless EGFR dimer transients (α1) is, thus, causing ultrasensitive phosphorylation responses at low ($\alpha_L < 0.1$) EGF receptor occupancy that occurs at physiological EGF concentrations. At $\alpha_L > 0.3$ autocatalytic ExAsym reactions ($\alpha_2 + \alpha_3$) mostly cause EGFR phosphorylation, to be taken over by catalytic liganded ExSym dimer reactions (ε_4) at α_L above 0.5 (Fig 5D).

The maximal dephosphorylation rates by RPTPγ (Γ1, Γ3) and constant dephosphorylation rates by TCPTP (Γ2, Γ4) are relative to catalytic and autocatalytic EGFR phosphorylation rates and were estimated in an unshared fashion among the corresponding expression perturbations and linked in the complementary (invariant) cases. Similarly, the EGFRp-mediated oxidative RPTPγ inhibition maximal rate (B) was linked among EmCit_WT and TCPTP KO and corresponding rescue because of RPTPγ and EGFR expression invariance and set to 0 for RPTPγ KO and p22^{Phox} KO. The EGFRp- and EGF-EGFRp-independent basal ratio of active (reduced) over inactive (oxidized) RPTPγ was measured and fixed among all experiments (k2/k1 = 0.08, Fig 3D). However, Γ1–Γ4 as well as B were left free for the fit of the endogenous EGFRp response in WT MCF7 that express an order of magnitude less EGFR relative to EmCit_MCF7 cells ($8 \pm 0.1 \times 10^3$ vs. $2.6 \pm 0.35 \times 10^5$ EGFR/cell). The maximal EGFRp (Γ1) and EGF-EGFRp (Γ3) dephosphorylation rates show that RPTPγ dephosphorylates ligandless EGFRp two-to-three orders of magnitude more efficient than liganded EGF-EGFRp (Fig 5E) in WT as well as in EmCit_MCF7 cells (Fig EV4D). RPTPγ, thus, primarily suppresses autocatalytic phosphorylation of ligandless EGFR, in line with our biochemical finding that RPTPγ interacts with unliganded monomeric EGFR and not liganded EGF-EGFR (Fig 4F). The constitutive TCPTP activity was 10-fold lower on

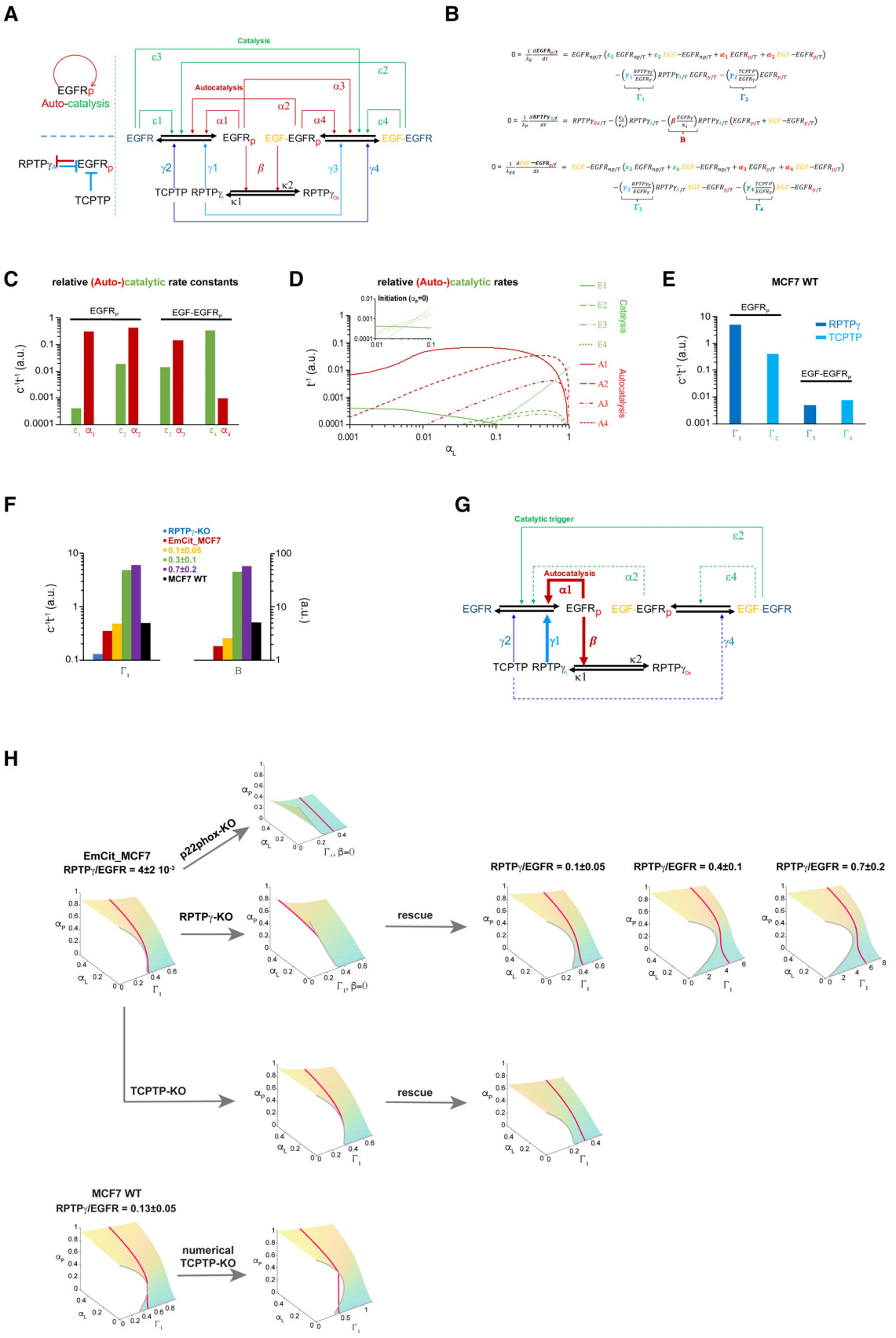

Figure 5.

Figure 5. RPTPγ-EGFR-TCPTP network reconstruction and bifurcation analysis.

A Full RPTPγ-EGFR-TCPTP network architecture depicting the chemical conversions (black arrows; p: phosphorylation on EGFR, Ox: oxidized catalytic cysteine on RPTPγ, A: active RPTPγ with reduced catalytic cysteine) and all possible regulatory interactions (colored arrows: causal links; $\varepsilon_1-\varepsilon_4$ corresponding catalytic, $\alpha_1-\alpha_4$ autocatalytic rate constant for EGFR phosphorylation (Fig EV4A)); γ_1 and γ_3 – second-order RPTPγ-specific, γ_2 and γ_4 – second-order TCPTP-dependent dephosphorylation; β – second-order EGFR-dependent oxidation of RPTPγ; κ_2 and κ_1 – intrinsic PTP deactivation and activation rate. Rate constants ($\varepsilon_1-\varepsilon_4, \alpha_1-\alpha_4, \gamma_1-\gamma_4, \beta$) are color coded as in (B–F) and Fig EV4A and B.

B Ordinary differential equations (ODEs) that describe the dynamics of the coupled reactants EGFRp, EGF-EGFRp and RPTPγ$_A$ in the general symmetric autocatalytic toggle switch model. $EGFR_{p/T}$, $RPTP\gamma_{A/T}$ and $EGF-EGFR_{p/T}$ describe the fractions of active (phosphorylated) proteins, relative to the respective total protein concentration. $EGFR_{np/T}$ and $PTP_{Ox/T}$ describe the fractions of inactive (non-phosphorylated or oxidized) proteins, EGF-EGFR depicts EGFR molecules liganded by EGF. $\Gamma_1, \Gamma_2, \Gamma_3, \Gamma_4$, B: fitted relative kinetic parameter groups color coded to their corresponding rate constants.

C Catalytic ($\varepsilon_1-\varepsilon_4$) and autocatalytic ($\alpha_1-\alpha_4$) rate constants obtained from iterative global fitting the ODEs in (B) solved for steady state ($dEGFR_{p/T}/dt = dEGF\text{-}EGFR_{p/T}/dt = dRPTP\gamma_{A/T}/dt = 0$) to EGF-dose response ($a_L-a_P$) data from all EGFR and PTP expression conditions (Fig 2E, F and I). EGFRp, EGF-EGFRp: product of the corresponding reactions.

D Relative catalytic (E_1-E_4) and autocatalytic (A_1-A_4) EGFR phosphorylation rates at steady state as a function of receptor occupancy (a_L). Steady state reaction rates were calculated by multiplication of the rate constants ($\varepsilon_1-\varepsilon_4; \alpha_1-\alpha_4$) by the relative abundance of the corresponding reactants and catalysts (EGFR, EGFRp, EGF-EGFR, EGF-EGFRp) obtained by the global fit. Inset: Calculation of the initiation of the signal by catalytic reactions (E_1-E_4) at $a_P = 0$, calculated by multiplication of rate constants ($\varepsilon_1-\varepsilon_4$) by the relative abundance of reactants (EGFR = $1-a_L$; EGF-EGFR = a_L).

E Maximal dephosphorylation rates by RPTPγ ($\Gamma_{1,3} = \gamma_{1,3}$. RPTPγ/EGFR$_T$; dark blue) or TCPTP ($\Gamma_{2,4} = \gamma_{2,4}$.TCPTP/EGFR$_T$; light blue) of ligandless EGFRp (Γ_1, Γ_2) or liganded EGF-EGFRp (Γ_3, Γ_4) obtained from iterative global fitting the ODEs in (B) solved for steady state ($dEGFR_{p/T}/dt = dEGF\text{-}EGFR_{p/T}/dt = dRPTP\gamma_{A/T}/dt = 0$) to EGF-dose response ($a_L-a_P$) data of MCF7 WT cells (Fig 2F).

F Change of the free parameter groups $\Gamma_1 = \gamma_1$RPTPγ/EGFR$_T$ and B = β EGFR$_T$/k1 in EmCit_MCF7 RPTPγ-KO (blue), EmCit_MCF7 (red), EmCit_MCF7 RPTPγ-KO expressing RPTPγ-mTFP splitted in three clusters with increasing RPTPγ-mTFP/EGFR-mCitrine ratio (yellow, green, purple; Figs 2H and EV2G) and WT MCF7 cells (black).

G RPTPγ-EGFR-TCPTP network architecture depicting the chemical conversions and regulatory interactions that are relevant for the EGFR-phosphorylation response at physiological ($a_L < 0.1$) EGF-concentrations. EGFR phosphorylation is mainly driven by autocatalysis among unliganded EGFR (α_1; see (D)). EGFRp oxidatively inactivates RPTPγ via ROS (β). RPTPγ counteracts this autocatalysis by dephosphorylation of EGFRp (γ_1). The autocatalytic activation needs to be triggered by a sufficient amount of EGFRp in the system that must come from (ε_2) and/or from ($\varepsilon_3, \varepsilon_4$), which produce EGF-EGFRp that can generate EGFRp via α_2. TCPTP ($\gamma_{2,4}$) has a comparably weaker, but constitutive modulatory dephosphorylation activity.

H Experimentally reconstructed 3D-bifurcation diagrams showing the dependence of steady-state EGFR phosphorylation (α_p) on Γ_1 (=γ_1.RPTPγ/EGFR) and EGF-receptor occupancy (α_L) for EmCit_MCF7 cells (left, 2nd row) with derivated p22phox-, TCPTP- and RPTPγ-KO and corresponding TCPTP- and RPTPγ-rescue cells, indicated by the black arrows. Last row: MCF7 WT cells (left) with a numerical knockout of TCPTP, (TCPTP associated rates Γ_2 and $\Gamma_4 = 0$). Molecular ratio of RPTPγ/EGFR are depicted on top of the corresponding diagram; red line: fit to the experimentally derived dose response trajectory.

ligandless EGFRp (Γ2) with respect to RPTPγ and exhibited a similar trend of less efficiently dephosphorylating EGF-EGFRp (Γ4). Liganded receptors will, thus, be persistent in their phosphorylation at the PM, while phosphorylation among ligandless receptors can only be maintained by EGFRp-mediated oxidative RPTPγ inhibition (B). Both maximal RPTPγ activity Γ1 and maximal EGFRp-mediated oxidative RPTPγ inhibition (B) increased with RPTPγ expression, demonstrating that the mutual inhibition between RPTPγ and EGFR is enhanced when their expression level becomes similar (Fig 5F). These results enable to construct the autocatalytic toggle switch reaction network that generates an ultrasensitive EGFR phosphorylation response at physiological EGF receptor occupancies < 0.1 (Fig 5G). The core of the system is the autocatalytic reaction among ligandless EGFR and EGFRp that generates more EGFRp that couples to NOX to oxidatively inhibit RPTPγ activity on EGFRp, further amplifying the autocatalytic phosphorylation of ligandless EGFRp once triggered by the EGF-dependent ExAsym catalytic reaction.

To assess how the steady-state EGFR phosphorylation response is established by the non-linear dynamics of the RPTPγ-EGFR-TCPTP system, 3D α_p (EGFRp + EGF-EGFRp) bifurcation profiles were reconstructed from the estimated parameters of the four expression variation groups (RPTPγ, TCPTP, p22Phox, and EGFR) as function of Γ1 = γ1 RPTPγ/EGFR and α_L input (Fig 5H; Materials and Methods). The bifurcation profile of EmCit_MCF7 cells that largely overexpress EGFR-mCitrine with respect to RPTPγ (RPTPγ/EGFR-mCitrine = $4 \pm 2 \times 10^{-3}$, EGFR$_T$ = $2.6 \pm 0.35 \times 10^5$) still exhibited a narrow S-shaped bistable dynamical signature of the toggle switch (Reynolds *et al*, 2003) and poising of the system at the criticality edge (Stanoev *et al*, 2020) of this narrow bistable region. This S-shape was lost upon RPTPγ or p22Phox KO. In the former case, the system was poised in a high pre-activated monostable state despite auxiliary PTP activity, showing that the dominant high activity of very lowly expressed RPTPγ ($1 \pm 0.2 \times 10^{-3}$ molecules/cell) maintains the low EGFR phosphorylation level in the absence of growth factor triggers. That is why in the latter p22^{Phox} KO case, where RPTPγ cannot be inhibited, the system is poised in an inactivated monostable state that only slightly increased with α_L. The RPTPγ KO RPTPγ-mTFP rescue to 40 ± 9-fold (mean ± SEM) that of endogenous level (RPTPγ-mTFP/EGFR-mCitrine = 0.1 ± 0.05), yielded a bifurcation profile with an enhanced bistable region as compared to EmCit_MCF7 cells and poising of the system close to criticality. Despite a 40-fold higher RPTPγ expression, Γ1 (Maximal RPTPγ activity) and B (maximal oxidative RPTPγ inhibition) were only slightly elevated, which points to a concentration dependent inhibitory RPTPγ mechanism, possibly dimerization (Kd ~ 3 μM; Barr *et al*, 2009). This RPTPγ density dependent inhibition might convey robustness in the EGFR phosphorylation response to RPTPγ expression level. At even higher RPTPγ-mTFP overexpression (140 ± 28 or 180 ± 38 fold (mean ± SEM) with respect to endogenous), leading to RPTPγ-mTFP approaching EGFR-mCitrine expression (RPTPγ-mTFP /EGFR-mCitrine = 0.4 ± 0.1 and 0.7 ± 0.2), both Γ1 and B strongly increased (Fig 5F). In these cases, RPTPγ's dominant overall dephosphorylating activity with respect to other PTPs together with a more effective EGFRp-coupled oxidative RPTPγ inhibition, accentuates RPTPγ-EGFR toggle switch dynamics, poising it close to the enlarged bistable region leading to a steep

ultrasensitive response (Fig 5H). On the other hand, TCPTP KO poised the system in the preactivated monostable state at the boundary of a slightly enlarged bistable region of EmCit_MCF7 cells. Upon TCPTP-mTFP rescue, however, the bistable region vanished, poising the system away from criticality in the monostable regime (Figs 5H and EV4E). This shows that constitutive phosphatase activity of the PM-proximal pool of ER-associated TCPTP is essential to maintain RPTPγ/EGFR toggle switch dynamics in the inactive state at the PM. MCF7 cells that endogenously express RPTPγ/EGFR = 0.13 ± 0.03 with only $8 \pm 1 \times 10^3$ receptors/cell exhibited a bifurcation profile with a pronounced S-shaped bistable dynamical signature of the toggle switch reminiscent of that of the RPTPγ-mTFP/EGFR-mCitrine = 0.1 ± 0.05 rescue cells. The poising of the system at the criticality edge enables a low threshold ultrasensitive response, generating responsiveness to very low-growth factor concentrations (Fig 5H). The robustness to preactivation at this sparse EGFR-RPTPγ expression is likely due to their interaction (Fig 4F) thereby matching maximal PTP activity to the overall autocatalytic phosphorylation rates. In addition, the effective EGFRp-mediated oxidative inhibition of RPTPγ (B = 5, Fig 5F) that causes the low threshold ultrasensitive response at this sparse expression, points at nanoscale EGFRp-RPTPγ-NOX clusters (Fig 4E) that effectively oxidize RPTPγ within the complex by molecular proximity to the ROS source (NOX1-3). Numerical KO of TCPTP activity clearly poises the RPTPγ/EGFR toggle switch system in the bistable region causing irreversible EGFR phosphorylation responses to growth factor triggers. RPTPγ-EGFR-TCPTP network dynamics is, thus, poised at the edge of bistability to respond highly *sensitive* to low level EGF stimuli in a reversible manner while being robust to noise.

RPTPγ is a suppressor of EGFR promigratory signaling response

In order to investigate how the RPTPγ-EGFR growth factor sensing network affects cellular phenotype in relation to EGF dose, we compared short-term (1 h) morphodynamic and signaling parameters to long-term migratory and proliferative parameters (12 h) in MCF7 WT, RPTPγ-KO, and $p22^{phox}$-KO cells.

We first compared the growth factor dependent morphodynamics of individual MCF7 WT cells to those in which either RPTPγ or $p22^{phox}$ was knocked out. EGF-induced PM shape-changes were measured over a period of an hour by time-lapse fluorescence microscopy of the PM marker BFP-tkRas (Schmick *et al*, 2014; Fig 6A). The ratio of the perimeter of an equiareal circle to the actual perimeter of the cell (P_{circle}/P_{cell}) was used as measure of cellular morphology. This morphometric parameter approaches one for a circular shape and lowers in case of enhanced overall curvature generated by protrusions. The distribution of (P_{circle}/P_{cell}) over time and all cells for a given condition allows the comparison of the ensemble of manifested morphologies between conditions.

In MCF7 WT cells, a low, physiological (1 ng/ml) EGF-stimulus caused the cells to switch from a relatively static to a highly dynamic morphing behavior with many protrusions (Fig 6A and B). This is consistent with promigratory signaling from EGF-triggered autocatalytically phosphorylated EGFRp monomers at the PM. In contrast, a high, receptor saturating EGF-stimulus (160 ng/ml) caused retraction and rounding, pointing towards onset of proliferation as previously described for high EGF stimulus (Brüggemann *et al*, 2021). RPTPγ-KO cells, however, exhibited already in the absence of stimulus highly dynamic morphing behavior with more protrusions as compared to WT (Fig 6A and B). This dynamic behavior was only slightly enhanced upon 1 ng/ml EGF-stimulus and was similar to that of WT cells stimulated with 1 ng/ml EGF. This is in agreement with constitutive promigratory signaling from constitutively autocatalytically phosphorylated EGFRp monomers at the PM in RPTPγ-KO cells. A high (160 ng/ml) receptor saturating EGF-stimulus still maintained the dynamic morphing behavior (Fig 6A), while additionally causing some retraction and rounding (Fig 6B). This is in agreement with the altered EGFR-trafficking in RPTPγ-KO cells that maintains a substantial fraction of liganded phosphorylated EGF-EGFRp on the PM that engage promigratory effectors (Brüggemann *et al*, 2021). As apparent from the higher median P_{circle}/P_{cell} and narrower distribution, $p22^{phox}$-KO cells exhibited less membrane protrusions as compared to WT cells (Fig 6B), consistent with RPTPγ constitutively suppressing EGFR phosphorylation (Fig 5H). However, 1 ng/ml EGF stimulus caused retraction and rounding in contrast to the very dynamic morphing behavior of WT cells (Fig 6A and B). This points towards onset of proliferation, similar to WT cells stimulated with 160 ng/ml EGF. This retraction persisted at high (160 ng/ml) stimulus, which corroborates the low dephosphorylating activity of RPTPγ on liganded EGF-EGFRp (Fig 5E) that can engage proliferative Erk signaling from EEs (Brüggemann *et al*, 2021). Indeed, a receptor non-saturating 20 ng/ml EGF stimulus generated a delayed Erk response at 30′ as compared to WT cells that exhibit a strong Erk activation peak at 5′ caused by autocatalytically phosphorylated ligandless EGFR at the PM (Fig 6C).

To assess if internalized EGF-EGFRp in $p22^{phox}$-KO cells indeed affects proliferative signaling, we measured phosphorylation of the S-phase blocker retinoblastoma protein (pRb) by immunofluorescence (Fig 6D). This showed a gradual increase of Rb phosphorylation in MCF7 WT cells with increasing EGF. In comparison to MCF7 WT cells, however, $p22^{phox}$-KO cells exhibited a hyperproliferative signaling response already at 1 ng/ml EGF, whereas RPTPγ-KO cells exhibited hypoproliferative signaling over the whole range of EGF stimuli (0–160 ng/ml). To directly measure the effect of $p22^{phox}$-or RPTPγ-KO on cell proliferation, clonogenic assays under sustained EGF (20 ng/ml and 0.5% FCS; Figs 6E and EV5A) or in complete serum growth medium with 10% FCS at three linear increasing cell seeding densities (1, 2, and 3-fold) were performed (Fig EV5B). By renormalizing the area occupied by cell colonies after 7 days to the cell seeding density, a measure of average colony size and thereby proliferation of cells was obtained (Klein *et al*, 2019). As evident from the normalized area occupied by cell colonies and in agreement with proliferative signaling (Fig 6D), $p22^{phox}$-KO and RPTPγ-KO cells exhibited significant hyper- and hypo-proliferative behavior with respect to WT cells, respectively (Fig 6E).

To next investigate how the EGFR-RPTPγ sensory system coordinates the balance between migration and proliferation in tissue regeneration, we used a simple unicellular MCF7 model system of wound healing (Cappiello *et al*, 2018; Brüggemann *et al*, 2021). For this, invasion of confluent monolayers of RPTPγ-KO and $p22^{phox}$-KO cells into a cell-free gap was monitored over 12 h after removal of a barrier (Figs 6F and EV5C, Movie EV1). The evolution of gap closure by the invading cell mass was determined by quantifying cell density in lateral bins (Fig 6F, second column, top; Materials and Methods). WT MCF7 cells showed virtually no migration into the

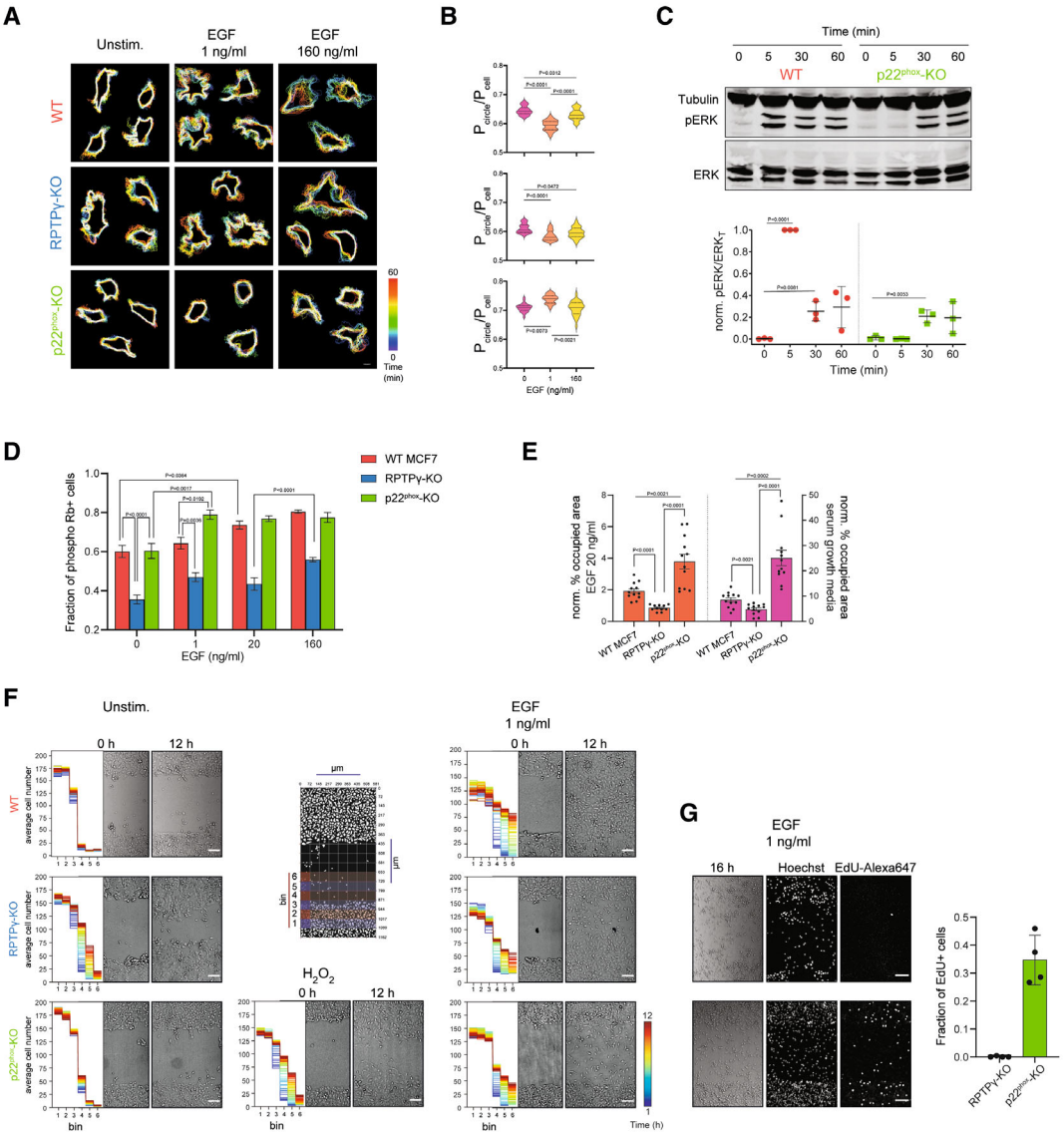

Figure 6. RPTPγ is a suppressor of promigratory EGFR-signaling at the plasma membrane.

A Representative cell contour maps showing the temporal changes (color bar: time (min), bottom right) in cell morphology for WT (upper row), RPTPγ-KO (middle row) and p22^{phox}-KO (bottom row) MCF7 cells, expressing PM-marker BFP-tkRas imaged every 2′ over 60′, without (1st column) or with 1 ng/ml (2nd column) or 160 ng/ml (3rd column) EGF-Alexa647. Scale bar: 10 μm.

B Morphometric quantification by the ratio of the perimeter of an equiareal circle to the actual perimeter of all cells ($N = 3$ biological replicates, $n = 9$–20 cells) at all timepoints (P_{circle}/P_{cell}). 1st row: WT, 2nd row: RPTPγ-KO, 3rd row: p22phox-KO MCF7 cells. *P*: one-way ANOVA with Šídák's multiple comparisons.

C Top: Representative Western blot against Erk and phosphorylated Erk (pT202 and pY204) in WT (red) compared to p22^{phox}-KO (green) MCF7 cells after the indicated times of sustained stimulation with 20 ng/ml EGF-Alexa647. Bottom: Corresponding quantification of the fraction of phosphorylated ERK as a function of stimulation time. Mean ± SD, $N = 3$ biological replicates, *P*: unpaired two-tailed *t*-test.

D Quantification of cell proliferation using retinoblastoma (Rb) protein phosphorylation detected by immunofluorescence, for WT (red), RPTPγ-KO (blue) and p22^{phox}-KO (green) MCF7 cells without or post 24 h of EGF-Alexa647 treatment (1, 20, 160 ng/ml). Mean ± SEM, $N = 3$ biological replicates, $n > 2{,}000$ cells per EGF stimulus per cell line, *P*: two-way ANOVA with Tukey multiple comparisons.

E Quantification of the culture-well area (%) occupied by proliferating cell-colonies, obtained from clonogenic assays of WT, RPTPγ-KO and p22^{phox}-KO MCF7 cells, plated either in medium containing 20 ng/ml EGF and 0.5% FCS (left: orange bars, $N = 3$–4 biological replicates, 11–12 wells each) or complete serum growth medium containing 10% FCS (right: pink bars, $N = 4$ biological replicates, 12 wells each). Mean ± SEM, *P*: unpaired two-tailed *t*-test with Welch's correction.

F Representative transmitted light micrographs of WT (top row), RPTPγ-KO (middle row) and p22^{phox}-KO (bottom row) MCF7 cells, without (1st column) and during stimulation with, H_2O_2 (0.5 mM, 2nd column) or EGF-Alexa647 (1 ng/ml, 3rd column) at the indicated times (0, 12 h) after removal of a migration barrier. Scale bar: 100 μm. Insets left of the images: Temporal maps (color-code lower right) depicting the average cell number (over $N = 4$–5 biological replicates) distributed in six spatial bins around the initial cell front measured every 10′ (schematic in second column: location of the lateral bins in the migration chamber).

G Left panel: Exemplary images of RPTPγ-KO (top row) and p22^{phox}-KO (bottom row) MCF7 cells stimulated with 1 ng/ml EGF-Alexa647, at 16 h after removal of a migration barrier together with Hoechst 33342 (2nd column) and 5-Ethinyl-2′-Desoxyuridin (EdU 10 μM, 1 h; 3rd column) staining obtained after 17 h. Right Graph: Quantification of the fraction of dividing (EdU^{+}) cells between 16th and 17th hour. $N = 4$ biological replicates, Mean ± SD.

gap under serum starvation conditions, whereas RPTPγ-KO cells exhibited autonomous migration into the gap in agreement with constitutive promigratory signaling from autocatalytically phosphorylated EGFRp monomers at the PM. However, whereas p22^{phox}-KO MCF7 cells showed virtually no migration into the gap, constitutive RPTPγ oxidation by 0.5 mM H_2O_2 in these cells phenocopied the autonomous migration of unstimulated RPTPγ-KO cells. This corroborates that EGFRp mediated oxidative inhibition of RPTPγ is a requisite for promigratory signaling via autocatalytic EGFR phosphorylation.

Upon constitutive stimulation with 1 ng/ml EGF the coordinated migration and proliferation of MCF7 WT cells filled and closed the gap within 12 h (Fig 6F). In contrast, a constitutive receptor saturating (160 ng/ml) EGF stimulus resulted in minor movement of the cell front and did not lead to gap closure, as previously described (Brüggemann *et al*, 2021; Fig EV5C and Movie EV1). The latter minor cell front progression is due to predominantly proliferative signaling (Fig 6D) from rapidly endocytosed EGF-EGFRp and only weak promigatory signaling from residual EGFRp at the PM.

The constitutive migration of RPTPγ KO cells was only slightly enhanced by 1 ng/ml EGF, with more individual cells being released from the migrating monolayer front (Fig 6F). This likely originates from additional promigratory signaling from liganded EGF-EGFRp that remains at the PM because of deregulated endocytosis and unidirectional trafficking of EGF-EGFR to LE's in these cells (Figs 4B and EV3C). That this disordered gap invasion was due to migration and not proliferation was further apparent from the virtual absence of Alexa647-labeled EdU- (5-ethynyl-2′-deoxyuridine-) incorporation into newly synthesized DNA after 16 h of migration into the gap (Fig 6G). In other words, proliferative EGF-EGFRp signaling from endosomes is minor in RPTPγ KO cells due to the deregulated endosomal trafficking of EGF-EGFRp (Figs 4B and EV3C). On the other hand, p22^{phox}-KO cells failed to consistently initiate a coordinated migratory response upon stimulation with 1 ng/ml EGF, maintaining the monolayer front at its original position from which individual cells migrated into the gap. This residual migration possibly occurs due to loss in cell–cell contact after cell rounding, which usually precedes proliferation in this hyperproliferative tissue. The defect migratory response of p22^{Phox} KO cells is also apparent from the temporal average cell profile (Fig 6F, left profiles) that exhibits a sustained discontinuity at the barrier position in contrast to that of RPTPγ KO cells. Furthermore, the average cell count before the barrier position was hardly affected in p22^{Phox} KO cells, whereas it decreased for RPTPγ KO cells. This indicates that solely migrating RPTPγ KO cells decrease the bulk cell mass before the barrier position, whereas proliferating p22^{Phox} KO cells sustain this cell mass despite individual cells escaping into the gap. EdU staining after 16 h clearly confirmed the hyperproliferative behavior of these cells already at 1 ng/ml EGF around and within the gap, increasing the number of cells over time that are, however, unable to close the cell-free gap within up to 16 h (Fig 6F and G). Due to strong proliferative signaling from endocytosed liganded receptors at 160 ng/ml EGF, a disordered p22^{Phox} KO cell front protruded further into the gap from which individual cells escaped to migrate into the gap.

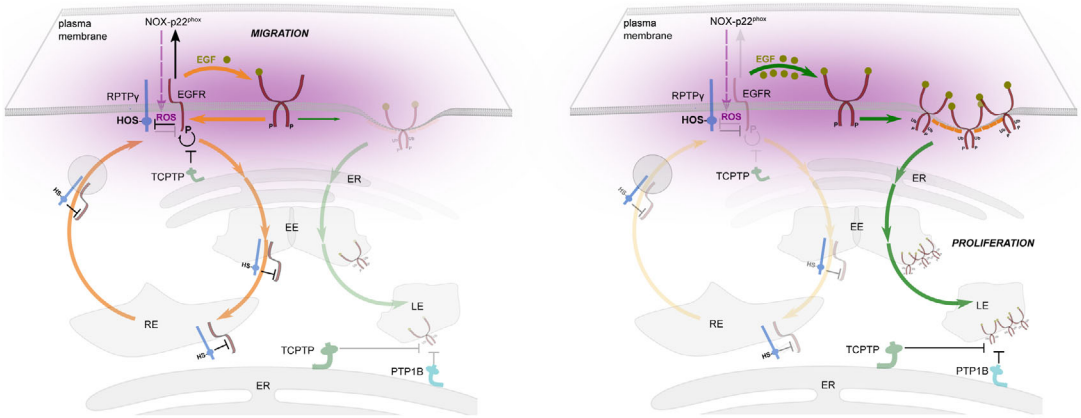

Figure 7. RPTPγ-EGFR-TCPTP growth factor sensory network dynamically established in space.

Left: The continuous recycling (orange circular arrows) of interacting RPTPγ-EGFR monomers through the reducing environment of the cytoplasm maintains the catalytic cysteine of RPTPγ in the reduced (SH) state, such that it continuously dephosphorylates spontaneously phosphorylated EGFRp monomers at the PM. Upon receptor subsaturating EGF stimulus (curved orange arrow), transient EGF-EGFR$_2$ dimers catalytically trigger (orange straight arrow) the autocatalytic phosphorylation reaction that generates EGFRp monomers at the PM (black circular arrow). EGFRp activate NOX complexes (black arrow to NOX-p22^{phox}) that produce H_2O_2 (purple cloud and dashed arrow) at and near the PM that oxidatively inactivates the inhibitory phosphatase activity of RPTPγ (oxidated catalytic cysteine: SOH) on ligandless phosphorylated EGFRp monomers. These signal and activate promigratory effectors at the PM. The toggle switch causality resulting from the EGFRp-mediated oxidative inhibition of RPTPγ and RPTPγ's dephosphorylating activity on EGFRp is represented by the mutual inhibitory arrows between interacting EGFR and RPTPγ. On the other hand, the constitutive dephosphorylation of EGFRp by the PM-proximal pool of endoplasmic reticulum associated TCPTP (green) maintains reversibility in the ultrasensitive EGFR phosphorylation response to EGF. The reactivation (catalytic cysteine reduction: SH) of the phosphatase activity of inactivated RPTPγ (oxidated catalytic cysteine: SOH) by vesicular recycling through the cytoplasm via the RE (curved orange arrows), together with vesicular recycling and dephosphorylation of ligandless EGFRp, reverts ligandless EGFRp to basal levels at the PM when growth factor levels decline. In dependence on EGF concentration (green arrow), accumulation of liganded EGF-EGFR in clathrin coated pits generate stable ubiquitinated (Ub) EGF-EGFR complexes that unidirectionally traffic to the LE via the EE (green arrow), from which they couple to proliferative effectors. High, receptor saturating, levels of EGF (right diagram) thereby lead to a faster accumulation of EGF-EGFR in endosomes, depletion of promigratory EGFRp monomers at the PM, and predominantly proliferative EGF-EGFR signaling from endosomes. In this branch, EGF-EGFRp signal duration is determined by the dephosphorylating activities of ER-associated TCPTP (green) and PTP1B (cyan) while the receptor complexes traffic to the LE via the EE.

The slightly enhanced proliferative signaling of RPTPγ KO cells at this high EGF concentration (Fig 6D), combined with enhanced promigratory signaling from liganded receptors that are sustained at the PM due to deregulated EGFR trafficking, also caused a disordered cell front to further protrude into the gap. These results thus demonstrate the role of RPTPγ in suppressing autonomous migration by suppressing autocatalytic EGFR phosphorylation at the PM in the absence of EGF (Figs 4B and EV3C) but not proliferation originating from endosomal EGF-EGFRp signaling at physiological EGF levels that result in < 5% receptor EGF-occupancy.

Discussion

We provide evidence that the ROS-mediated toggle switch coupling of RPTPγ to autocatalytic EGFR monomer phosphorylation enables promigratory ultrasensitive phosphorylation responses at the PM to physiological EGF stimuli at which a very minor fraction of EGFR is bound by EGF (< 5%). The short lived (1–10s) EGFR dimer reaction intermediates (Chung *et al*, 2010; Low-Nam *et al*, 2011; Koseska & Bastiaens, 2020; Salazar-Cavazos *et al*, 2020) enable this dynamic reaction system to be sensitive to such low EGF concentrations. The phosphorylation response largely exceeds the number of liganded EGF-EGFR and is driven by the autocatalytic ligandless EGFR phosphorylation reaction (EGFRp-EGFR-> 2EGFRp; Reynolds *et al*, 2003; Baumdick *et al*, 2018; Stanoev *et al*, 2018; Koseska & Bastiaens, 2020) that we found to be three orders of magnitude more efficient than the catalytic ligandless reaction (EGFR-EGFR-> EGFRp). The high catalytic activity of RPTPγ that we have shown to specifically interact and fully dephosphorylate ligandless EGFRp, necessitates EGFRp-mediated NOX1-3 activation to oxidatively inhibit RPTPγ in order to induce an autocatalytic phosphorylation response. We could show that low level EGF triggers this autocatalytic reaction via the catalytic formation of EGFRp by asymmetric (EGF-EGFR$_2$; Alvarado *et al*, 2010; Liu *et al*, 2012) dimer transients. Once initial EGFRp exceeds a threshold, the system approaches a new steady state of amplified EGFRp phosphorylation, now keeping RPTPγ in its oxidized, inactive form. Experimental bifurcation analysis of linked expression perturbations experiments revealed that constitutive activity of PM-proximal ER-associated TCPTP poises RPTPγ/EGFR toggle switch dynamics at the critical edge of bistability (Stanoev *et al*, 2020) to respond highly sensitive to low level EGF stimuli in a reversible manner while being robust to noise. EGFR-RPTPγ vesicular recycling through the reducing cytoplasm thereby closes the coupled redox- and dephosphorylation–phosphorylation cycles, enabling reset of the system to basal levels when growth factor levels decline (Fig 7, yellow curved arrows).

This autocatalytic EGFR toggle-switch signaling system at the PM is distinct from the liganded EGF-EGFRp monomers that form the more stable homotypic complexes that accumulate in clathrin coated pits. Due to the orders of magnitude lower catalytic activity of RPTPγ on EGF-EGFRp with respect to EGFRp (Fig 5E), these EGF-EGFRp clusters are preferentially ubiquitinated by the ubiquitin ligase cbl (Levkowitz *et al*, 1998; Soubeyran *et al*, 2002; Baumdick *et al*, 2015), endocytosed and engage proliferative signaling from endosomes via the soluble Erk pool (Stallaert *et al*, 2018; Brüggemann *et al*, 2021; Fig 7, green curved arrows). This branch of internalized proliferative EGFR signaling depletes the recycling EGFR pool in dependence on EGF concentration and EphR-mediated cell–cell contact signals that redistribute EGFR to EEs, enabling context dependent proliferative responses (Stallaert *et al*, 2018) in an evolving tissue. This EGF-EGFRp signaling from endosomes is neither dependent on NOX activity nor on interaction with RPTPγ and the temporal signaling response is determined by ER-associated TCPTP and PTP1B phosphatase activities while EGF-EGFR receptor complexes unidirectionally traffic to the LE (Haj *et al*, 2002; Yudushkin *et al*, 2007; Stanoev *et al*, 2018). RPTPγ is, thus, a suppressor of oncogenic migratory EGFR signaling from the PM but not that of proliferative signaling of endocytosed ubiquitinated receptor complexes. Our results provide support that the reaction dynamics of spatial–temporally organized tyrosine-kinase/PTP networks enable paracrine communication at physiological growth factor levels necessary for the regulation of collective tissue behavior.

Materials and Methods

Antibodies

Primary antibodies

rabbit anti-RPTPγ (rb-RPTPγ-P4: gift from C. Sorio, Department of Pathology, University of Verona, Verona, Italy, (Sorio *et al*, 1995)), mouse anti-TCPTP (MAB1930, R&D Systems, Minneapolis, MN), mouse anti-p22^{phox} (ab80896, Abcam, Cambridge, UK), anti-cysteine sulfenic acid 2-thiodimedone (ABS30, Merck, Darmstadt, Germany), living colors mouse anti-GFP (632381, Clontech, Mountain View, CA), goat anti-GFP (ab5450, Abcam), rabbit anti-phospho EGFR Y1068 (3777, Cell Signaling Technology, Danvers, MA), mouse anti-phospho EGFR Y1068 (2236, Cell Signaling Technology) rabbit anti-EGFR (4267, Cell Signaling Technology), goat anti-EGFR (AF231, R&D Systems), rabbit anti-phospho-ERK-1/2 Thr/Tyr 202/204 (9101, Cell Signaling Technology), mouse anti-ERK1/2 (ab366991, Abcam), rabbit anti-phospho-Akt Ser473 (9271, Cell Signaling Technology), mouse anti-Akt (pan) (2920, Cell Signaling Technology), rabbit anti-EEA1 (3288, Cell Signaling Technology), rabbit anti-Rab7 (9367, Cell Signaling Technology), rabbit anti-Rab11a (2413, Cell Signaling Technology), rabbit phospho-Rb Ser807/811 (8516, Cell Signaling Technology), mouse anti-GAPDH (CB1001, Merck), mouse anti-α-Tubulin (T6074, Merck), mouse anti-Na^+/K^+ ATPase-α3-subunit (BML-SA247-0100, Enzo Life Sciences, NY).

Secondary antibodies

IRDye 680 donkey anti-mouse IgG, IRDye 800 donkey anti-rabbit IgG, (LI-COR Biosciences, Lincoln, NE); Alexa Fluor 647 chicken anti-rabbit IgG, Alexa Fluor 647 donkey anti-goat IgG, Alexa Fluor 568 donkey anti-rabbit IgG (Life Technologies, Darmstadt, Germany).

Plasmids

The constructs, PTPRG-mCitrine/-mTFP/-mCherry, PTPN2-mCitrine/-mTFP, and EGFR-mCitrine/-mTFP/-mCherry, PTB-mCherry were generated previously (Stanoev *et al*, 2018). To create the PM-marker BFP-tkRas, the fluorescent protein BFP was fused to the 'tail of KRas', i.e. the C-terminal hypervariable region responsible for the PM-localization of Kras (KRas4B amino acids 169–188; Hancock *et al*, 1990; Schmick *et al*, 2014).

Cell culture and transfections

MCF7 cells (86012803, ECACC) were cultured in Dulbecco's modified Eagle's medium (DMEM; PAN-Biotech GmbH, Aidenbach, Germany) supplemented with 10% fetal bovine serum (FBS; PAN-Biotech GmbH), 2 mM L-Glutamine and 1% nonessential amino acids (NEAA, PAN-Biotech GmbH). Cells were transfected 24 h prior to the experiment with cDNA of interest with Fugene6 following the protocol of the manufacturer (Roche Diagnostics, Burgess Hill, UK). MCF10A cells (CRL-10317, ATCC) were grown in DMEM/F12 (PAN-Biotech GmbH) supplemented with 5% horse serum (Sigma–Aldrich Chemie GmbH, Munich, Germany), 20 ng/ml EGF, 500 ng/ml hydrocortisone (Sigma–Aldrich Chemie GmbH), 100 ng/ml cholera toxin (Sigma–Aldrich Chemie GmbH), 10 μg/ml insulin (Sigma–Aldrich Chemie GmbH). HT29 cells (HTB-38, LGC Genomics GmbH) were cultured in Ham's F12 culture medium (PAN-Biotech GmbH) supplemented with 2 mM L-Glutamine, 1% (NEAA) and 10% FBS. Cells were transfected with Lipofectamine 3000 following the protocol of the manufacturer (Life Technologies). The culture medium was exchanged 7 h after transfection. All cells were grown at 37°C in 5% CO_2 and regularly checked for mycoplasma (MycoAlert mycoplasma detection kit, Lonza, Basel, Switzerland). Identity of all cell lines was confirmed by STR analysis (Leibniz Institute DSMZ GmbH, Braunschweig, Germany). Cells were serum starved for at least 6 h prior to the experiment with respective culture media containing 0.5% FBS. The consistency of plasmid expression throughout different experiments was ensured by transfecting 80 ng of each plasmid per well of an 8-well Lab-Tek™ chambered cover glass slides (0.8 cm^2 surface area, ThermoFisher), and the amount of plasmid was scaled up proportional to the culture-well surface area for other culture-plates used. EGFR and PTPs were co-transfected with 1:1 DNA ratio. In PTB-FLIM experiments, a ratio of 1:2 was used for EGFR-mCitrine:PTB-mCherry.

Generation of gene knock-outs using CRISPR/CAS9

pSpCas9(BB)-2A-GFP (PX458) was a gift from Feng Zhang (Addgene plasmid #48138; http://n2t.net/addgene:48138; RRID:Addgene_48138). The oligonucleotides containing CRISPR guide RNA sequences (sgRNA) were designed (https://portals.broadinstitute.org/gppx/crispick/public) and synthesized (Sigma–Aldrich Chemie GmbH). sgRNA sequences used to create CRISPR KO cell lines are: PTPRG exon 7: 5'-TCCACTATTTCGCTACACGG-3′; PTPN2 exon 6: 5'-AGGGACTCCAAAATCTGGCC-3′; CYBA exon 2: 5'-GTAGGCACCAAAGTACCACT-3′. The sgRNAs were cloned into the BbsI site of the pX458 expression vector as described previously (Ran *et al*, 2013). MCF7 cells were plated on six well tissue culture dishes (SARSTEDT AG & Co. KG, Nümbrecht, Germany) and transfected with 2 μg of each pX458 construct using Fugene6. Cells were FACS sorted 24 h post-transfection using GFP expression, and single cells were sparsely seeded on 15 cm dishes to form separated clonal colonies. Single clone derived colonies were picked, expanded, and evaluated for knockout by western blot analysis.

EGF-Alexa647 and EGF-DyLight405

The His-CBD-Intein-(Cys)-hEGF-(Cys) plasmid was kindly provided by Prof. Luc Brunsveld, University of Technology, Eindhoven. Human EGF was purified from *E. coli* BL21 (DE3) and N-terminally labeled with Alexa647-maleimide or DyLight405-Maleimide as described previously (Sonntag *et al*, 2014) and stored at −20°C in PBS.

Synthesis and purification of DyTo

DyTo was formulated by labeling DYn2 with atto-590azide by azide-alkyne Huisgen cycloaddition (Rostovtsev *et al*, 2002). The reaction was performed by mixing the following reagents at the mentioned final concentrations to obtain 1 ml reaction volume. atto-590azide (6 mM, ATTO-TEC GmbH, Siegen, Germany) dissolved in DMSO was mixed with aqueous solution of click-chemistry grade $CuSO_4$ (40 mM, Jena Bioscience GmbH, Germany) and TCEP (40 mM, Sigma–Aldrich Chemie GmbH) for 5′. TBTA (20 mM, Sigma–Aldrich Chemie GmbH) was added to the mixture followed by the addition of DYn2 (18 mM, Cayman Chemical, MI, USA) dissolved in DMSO. The reaction was allowed to proceed overnight at room temperature in dark on a rocking platform.

DyTo was separated from the unreacted reagents and by-products by mass-directed preparative HPLC (infinity prep II, Agilent Series 1260, LC-MSD) using reversed-phase C18 column (VP10/125 5 μm) with a constant flow of 20 ml/min. Water/Acetonitrile (H_2O + 0.1% v/v TFA, CH_3CN + 0.1% v/v TFA) system was used as eluent. The product identity was verified on mass spectrometer integrated with HPLC system. The DyTo fraction obtained from the HPLC was subject to reduced-pressure evaporation, and the final product was obtained as dry-powder that was stored at −20°C.

Immunoprecipitation and western blots

Cells grown in 6-well tissue culture plates (SARSTEDT) were treated as per the experimental requirement and lysed using RIPA cell lysis buffer (50 mM Tris–HCl pH 7.9, 150 mM NaCl, 1% IGEPAL, 0.5% Na-deoxycholate, 20 mM NEM) supplemented with Complete Mini EDTA-free protease inhibitor (Roche Applied Science, Heidelberg, Germany) and phosphatase inhibitor cocktail 2 and 3 (1:100, P5726 and P0044, Sigma–Aldrich). For immunoprecipitation (IP), equal amounts of protein lysates were incubated with pull-down antibody overnight at 4°C followed by 2 h treatment with Dynabeads Protein G magnetic beads (10004D, ThermoFisher, MA) for pull down. Total and IP protein were prepared in XT Sample Buffer (1610791, Bio-Rad, CA) supplemented with 0.05 M DTT. The protein bands were resolved by SDS/PAGE using NuPAGE Novex 4–12% Bis-Tris gels (ThermoFisher) in MOPS-SDS running buffer (ThermoFisher) at 200 V constant voltage, blotted to polyvinylidene difluoride membrane by wet-tank transfer for 1.5 h at 100 V constant voltage and blocked with intercept (TBS) blocking buffer (LI-COR Biosciences) for 1 h.

Primary antibody incubation was performed over night at 4°C, followed by washing with TBS/T and incubation with the respective secondary antibodies for 1 h in the dark. After final washing with TBS/T, the blot was scanned using an Odyssey Infrared Imaging System (LI-COR). The integrated intensities of the protein bands on western blots were measured using the gel analyzer tool in Fiji (Schindelin *et al*, 2012), and signals of phosphorylated proteins were normalized to the integrated intensity of the corresponding

total protein bands. Protein bands of RPTPγ and RPTPγ-mCitrine were normalized to a loading control (Na^+/K^+-ATPase).

co-IP of EGFR upon RPTPγ-mCitrine (1st row: lanes 1–6) or RPTPγ^{C1060S}-mCitrine (lane 7) pull-down was performed with a goat anti-GFP antibody (ab5450, Abcam) from lysates of MCF7 cells co-transfected with EGFR and RPTPγ-mCitrine or RPTPγ^{C1060S}-mCitrine. Total protein concentrations of RPTPγ-mCitrine and EGFR in the lysate were measured by western blot as input control for the Co-IP. Co-immunoprecipitated EGFR was ratiometrically quantified over pulled down RPTPγ-mCitrine or RPTPγ^{C1060S}-mCitrine protein bands.

Confocal laser scanning microscopy (CLSM)

Cells were cultured and transfected (as described above) for confocal laser scanning microscopy (CLSM) experiments on 4 or 8-well Lab-Tek™ chambered cover glass slides (ThermoFisher). Before imaging, the culture media was replaced with phenol red-free DMEM supplemented with 25 mM HEPES (PAN-Biotech GmbH). Confocal images were acquired using a Leica TSC SP8 microscope (Leica Microsystems, Wetzlar, Germany), equipped with an environment-controlled chamber (Life Imaging Services) set to 37°C, a 405-nm diode laser and a white light laser (white light laser Kit WLL2, NKT Photonics). Imaging was done with HC PL APO CS2 63×/1.4NA oil immersion objective and pinhole between 1 and 1.7 airy units. Following excitation wavelengths were used for proteins with fluorescent fusion tags/labels: BFP/DyLight 405 (405 nm), TFP (458 nm), mCitrine (514 nm), mCherry/Alexa Fluor 568 (561 nm), Atto-Tec 590 (593 nm), Alexa Fluor 647 (640 nm). Fluorescence emission was detected by hybrid detectors (HyD) restricted at: BFP/DyLight 405 (415–450 nm), TFP (468–485 nm), mCitrine (524–560 nm), mCherry/Alexa Fluor 568 (571–620 nm), Atto-Tec 590 (605–630 nm), Alexa Fluor 647 (655–690 nm). About 12-bit images were recorded by frame-by-frame sequential scanning at 512 × 512 pixels, with 80 Hz scanning frequency.

Immunofluorescence

Cells grown in 4 or 8-well Lab-Tek™ chambered cover glass slides (ThermoFisher) were fixed with 4% PFA (15710, EM-grade, EMS, Hatfield, PA) in TBS (v/v) for 10′. Cells were permeabilized with 0.2% Triton X-100 (v/v) for 8′. Background staining was blocked by 1 h incubation with Intercept (TBS) Blocking Buffer at room temperature. Samples were incubated with primary antibodies at 4°C overnight and secondary antibodies for 1 h at room temperature. Antibodies were diluted in Intercept (TBS) Blocking Buffer. All washing steps following fixation, permeabilization, primary, or secondary antibody incubation were performed with TBS.

The extent of co-localization in CLSM images of the endosomal marker proteins (EMP): Rab11a, EEA1, or Rab7 with the protein of interest (POI): RPTPγ-mCitrine or EGFR-mCherry was computed in Fiji (Schindelin *et al*, 2012) by defining ROIs in EMP and POI channels by intensity thresholding in background-subtracted images. The EMP mask was converted to a binary mask and multiplied with the thresholded POI image. The integrated intensity from this overlapping area was normalized to the total integrated intensity of POI in the whole cell to obtain the fraction of POI co-localized to the EMP.

To determine the fraction of cells positive for Rb phosphorylation, cell nuclei stained with anti-phospho-Rb and Hoechst 33342 were detected with cellular segmentation algorithm Cellpose (Stringer *et al*, 2021) from the confocal images of respective staining. The number of cell nuclei positive for anti-phospho-Rb was normalized to the total number of nuclei detected with Hoechst 33342.

Fluorescence lifetime imaging microscopy (FLIM)

TCSPC FLIM of EGFR-mCitrine/PTB-mCherry or PTP-mCitrine/DyTo was performed at 37°C on the Leica SP8 laser-scanning microscope equipped with a fast lifetime contrast module (FALCON, Leica Microsystems) using the 63×/1.4NA oil objective. mCitrine was excited using the white light laser at a frequency of 20 MHz and wavelength of 514 nm, and fluorescence emission was collected between 525 to 560 nm on HyDs. The photon collection was split among 2–3 HyDs with an AcoustoOptical Beam Splitter (AOBS). Photons were integrated for a total of approximately 15–20 s per image (~300–600 photons/pixel, sum of all detectors) using the FALCON system.

The donor (mCitrine) count images were thresholded above the background fluorescence. Global analysis was performed as described previously (Grecco *et al*, 2009, 2010) by a custom script implemented in Python to deduce the spatial distribution of the fraction of FRET-exhibiting donor for EGFR-phosphorylation (PTB-mCherry bound fraction of EGFR-mCitrine: α_p) and PTP-oxidation (DyTo-bound fraction of PTP-mCitrine: α_{ox}).

Quantification of EGF-binding to WT MCF7 cells

WT MCF 7 cells were seeded in Lab-Tek™ chambered cover glass slides (ThermoFisher) with 10^5 cells per well 1 day before the experiment, to reach a confluent layer of cells at the day of the experiment. The cells were starved for 6 h in DMEM supplemented with 2 mM L-Glutamine and 1% nonessential amino acids but only 0.5% FCS. Before the start of the experiment, this medium was replaced with phenol red-free DMEM supplemented with 25 mM HEPES (PAN-Biotech GmbH). Cells were then stimulated at 37°C with different concentrations (0, 20, 80, 160 ng/ml) of EGF-Alexa647 plus Hoechst33342 (4 μM) in the same medium for 5′. They were washed 2× quickly with the same medium without EGF and Hoechst at 37°C and directly transferred to the microscope. Three to five fields of view were recorded with 5′ after stimulation using a 60×/1.35NA oil immersion objective at an Olympus IX81 widefield epifluorescence microscope (Olympus GmbH, Hamburg, Germany) equipped with a LED-illumination system (Spectra3; Lumencor, Beaverton, OR, USA) and an Orca™-Quest qCMOS™ camera (Hamamatsu Photonics K.K., Hamamatsu City, Japan). Hoechst33342 was imaged with 395/25- and 440/20-nm bandpass filters for excitation and emission light, respectively. Alexa647 was imaged using 635/22- and 680/42-nm bandpass filters for excitation and emission light. The fluorescence intensity in each Alexa647-image was quantified using Fiji (Schindelin *et al*, 2012) and normalized by the number of nuclei in each corresponding Hoechst33342 image. The mean background fluorescence value obtained from samples treated without EGF-Alexa647 was subtracted.

Fluorescence photoactivation microscopy

Fluorescence photoactivation microscopy was carried out at 37°C on a Leica SP8 microscope using a 63×/1.4NA oil objective. Cells were transfected with photoactivatable paGFP-RPTPγ and RPTPγ-mCherry, with or without co-expression of BFP-Rab11a. Pre-and post-photoactivation images were acquired for paGFP-RPTPγ and RPTPγ-mCherry using 488 and 561 nm laser excitation, respectively. For photoactivation, paGFP-RPTPγ was excited with the 405 nm diode laser at 80% transmission in three frames on a perinuclear region of interest (ROI) exhibiting RPTPγ-mCherry fluorescence. In the post-activation step, fluorescence images for paGFP-RPTPγ and RPTPγ-mCherry were acquired with a time interval of 30″, using the 488 nm and 561 nm WLL laser at 10% power. At the end of the experiment an image of BFP-Rab11a was acquired with 5% 405-laser power.

Following background correction, fluorescence gain on the PM was quantified by the ratio of local (cell periphery) paGFP-RPTPγ to RPTPγ-mCherry fluorescence using Fiji (Schindelin *et al*, 2012).

Spatial–Temporal maps

CSLM images obtained from WT MCF7 cells expressing EGFR-mCherry, RPTPγ-mCitrine and CBL-BFP at 1′ interval were background corrected prior to further processing. PM and nuclei in individual cells were masked using RPTPγ-mCitrine and CBL-BFP fluorescence, respectively. For each pixel in the cell space, the normalized radial localization (r) was calculated as follows:

$$r = \frac{r_{PM}}{r_{PM} + r_{NM}}$$

where r_{PM} and r_{NM} are the shortest Euclidean distances from each pixel to the PM and NM, respectively. The pixels were segmented in 10 radial bins based on their normalized distances. The mean fluorescence intensities were calculated in each segment for RPTPγ-mCitrine, EGFR-mCherry, and EGF-Alexa647 to obtain their spatial distribution profiles at each time point for individual cells. The spatial profiles obtained at consecutive time-points were concatenated to form 3D STMs and then combined to yield an average STM (Stanoev *et al*, 2018).

Fluorescence anisotropy microscopy

Fluorescence anisotropy microscopy was performed before and during EGF stimulation (160 ng/ml) in WT or RPTPγ-KO MCF7 cells ectopically expressing EGFR-QG-mCitrine (Baumdick *et al*, 2015). Cells were incubated in cell culture medium with 0.5% FCS for at least 6 h before the experiment. The microscope consisted of an Olympus IX-81 body equipped with a MT20 illumination system, a 20×/0.7NA objective and CellR software (Olympus GmbH, Hamburg, Germany). A linear dichroic polarizer (Meadowlark Optics, Frederick, Frederick, CO, USA) was placed in the illumination path of the microscope, and two identical polarizers in an external filter wheel were used to measure parallel (I_{II}) and perpendicular ($I_{\perp}$) polarized emitted light in two separate images. Steady state anisotropy (r_i) was calculated in each pixel i:

$$r_i = \frac{I^i_{II} - G^i I^i_{\perp}}{I^i_{II} + G^i\, 2I^i_{\perp}}$$

The G factor (G^i) was determined by acquiring the ratio of the intensities at perpendicular and parallel orientations for fluorescein in solution, which has a steady-state anisotropy close to zero due to its fast rotation. Quantification of anisotropy was performed using Fiji (Schindelin *et al*, 2012).

Super-resolution radial fluctuation (SRRF) under ultrarapid cryo-arrest

Ultra-rapid cryo-arrest of a stable MCF7 cell line expressing SNAP-EGFR and RPTPγ-mCitrine was done as recently described (Huebinger *et al*, 2021). For this, the cells were grown on fibronectin-coated (5 μg/cm^2, F0895, Sigma–Aldrich) circular microscopy cover slides (No.1; ∅ 4 mm) that were mounted to chambers from biocompatible silicone (4-well micro-Inserts; ibidi GmbH, Gräfelfing, Germany). Before the experiment, Snap-EGFR was labeled with 0.5 μM Snap-Surface Alexa647 (New England Biolabs GmbH, Frankfurt, Germany) for at least 60′. The cover slides were mounted to the ultra-rapid cryo-arrest device (Huebinger *et al*, 2021), which was placed on top of an epifluorescence microscope. The cells were cryo-arrested during observation on the microscope. The microscope consisted of an IX-83 microscope body equipped with a 40×/0.95NA objective (UPlanApo) and a MT20 illumination system (Olympus Deutschland GmbH, Hamburg, Germany) as well as an Orca-R2 camera (Hamamatsu Photonics, Hamamatsu, Japan). Series of 100 widefield fluorescence images were acquired for SRRF reconstructions of mCitrine (excitation: 470/40 nm; dichroic mirror 495 nm; emission 520/35 nm) and Alexa647 (excitation: 620/60 nm; dichroic mirror 640 nm; emission 700/75 nm) with pixel length of 163 nm and a frame rate of 1 frame/s. SRRF reconstruction was done using the NanoJ plugin (Laine *et al*, 2019) to Fiji (Schindelin *et al*, 2012).

Quantification of relative and absolute EGFR- and RPTPγ-expressions

Relative expression of EGFR in WT MCF7, EmCit_MCF7, and MCF10A cells was measured by EGF-Alexa647 binding to these cells (Stanoev *et al*, 2018). For this, cells were serum starved (0.5% FCS) for 6 h and subsequently treated for 5 min with 160 ng/ml EGF-Alexa647 and imaged by CLSM. The measured Alexa647 intensity was background subtracted and normalized to the background of untreated cells and reflects relative abundances of EGFR in individual cells of these three cell lines (Fig 2A). Since expression of EGFR in MCF10A (~10^5 receptors/cell) is known from the literature (Basolo *et al*, 1992), the relative expressions can be translated into absolute number of molecules. The simultaneously measured EGFR-mCitrine intensity in EmCit_MCF7 cells, thus, yields number of EGFR molecules per EGFR-mCitrine fluorescence ($2.6 \pm 0.3 \times 10^5$, mean ± SEM).

To get RPTPγ/EGFR ratios and molecular numbers out of fluorescence intensities, we used this information and a normalization procedure of the measured fluorescence intensity (I) of a fluorescently labeled cell subtracted and normalized by the mean background fluorescence of untransfected cells (BG). The fluorescence stemming only from the fluorophores (I–BG) is produced by a number of fluorophores (n) that emit fluorescence based on their intrinsic molecular

brightness, for the given excitation wavelength and corrected for the fraction of photons collected by emission filter settings (mb) and as a factor of instrument settings (k) that include excitation intensity and photon collection efficiency. BG contains the same factor with intrinsic cellular fluorophores n_{BG}, that have a molecular brightness mb_{BG}, which is different from mb, but in the same channel share k with (I–BG). By normalizing (I–BG) by BG we get:

$$\frac{(I-BG)}{BG} = \frac{k\ mb\ n}{k\ mb_{BG}\ n_{BG}} = \frac{mb\ n}{mb_{BG}\ n_{BG}}$$

Using this normalization procedure, the instrument factor k cancels out and normalized fluorescence is independent on the instrument used, except for excitation wavelength and emission wavelength filtering. In the case of EmCit_MCF7 cells, we have determined the average number of EGFR (n_{EGFR}) by the above-mentioned EGF-Alexa647-labeling in relation to MCF10A to be $2.6 \pm 0.3 \times 10^5$ (Fig 2A). Together with the measured average values for (I–BG)/BG on a large sample (59 ± 6, mean ± SEM; $n = 102$), we can determine the factor ($\mathrm{mb}^{-1}\ mb_{BG}\ n_{BG}$) to be $n_{\mathrm{EGFR}}/59 = 4.4 \times 10^3 \pm 0.6 \times 10^3$ (mean ± SEM). Thus, we get for the mCitrine channel independent on other instrument settings then excitation and emission wavelengths

$$\frac{(I_{mCit} - BG_{mCit})}{BG_{mCit}} 4.4 * 10^3 = n_{mCit}$$

This allows not only to calculate the number of EGFR in a smaller sample EmCit-MCF7 cells but also to deduce the average number of transiently transfected RPTPγ-mCitrine ($1.0 \pm 0.1 \times 10^5$, mean ± SEM) measured by widefield microscopy, but similar excitation and emission wavelength (widefield excitation: 461–489 nm, emission: 502–538 nm; confocal excitation: 514 nm, emission: 524–560 nm). Using this number and the measured (I_{mTFP}–BG_{mTFP})/BG_{mTFP} for RPTPγ-mTFP, we can determine the factor ($\mathrm{mb}^{-1}\ mb_{BG}\ n_{BG}$) for the TFP channel to be $4.7 \pm 0.9 \times 10^3$.

$$\frac{(I_{mTFP} - BG_{mTFP})}{BG_{mTFP}} 4.7 * 10^3 = n_{mTFP}$$

The close matching of the correction factor for mCitrine and mTFP shows that the factor ($\mathrm{mb}^{-1}\ mb_{BG}\ n_{BG}$) is actually very small for mTFP and mCitrine, which have very comparable molecular brightnesses, in the excitation and emission wavelength used. With this, we can derive the number of RPTPγ-mTFP molecules per cell ($1.0 \pm 0.2 \times 10^5$, mean ± SEM). This number matches very closely the number of RPTPγ-mCitrine (Fig 2G), which is the same construct with exchange fluorescent protein that has been transfected in the same way, validating the normalization procedure. Endogenous RPTPγ per cell was estimated from the ratio of RPTPγ-mCitrine to endogenous RPTPγ expression obtained by western blot (100 ± 15-fold; mean ± SEM; $N = 4$, $n = 7$; Fig EV2H).

Single cell morphodynamics

WT, RPTPγ-KO, and p22^{phox}-KO MCF7 cells were seeded on Lab-Tek™ chambered cover glass slides (ThermoFisher), transfected with EGFR-mCitrine or BFP-tkRas and incubated in cell culture medium with 0.5% FBS for at least 6 h before the experiment. Cells were stimulated with sustained doses of EGF-Alexa647 (1 or 160 ng/ml), and CLSM images were obtained every 2′ for 60′.

For the analysis of single cell morphodynamics, cells within dense colonies were excluded. Temporal stacks from EGFR-mCitrine or BFP-tkRas fluorescence images were segmented to binary masks: If necessary, a local contrast normalization (40 px, Integral Image Filters plugin (Schindelin *et al*, 2012)) was performed, and an Otsu automated intensity threshold applied. Masks were manually checked and corrected, cleaned, and split into single cell masks, from which area, and perimeter were measured. Morphometric changes were calculated using a Perimeter-Ratio:

$$\frac{Perimeter_{Circle}}{Perimeter_{Cell}} = \frac{2\pi \times \sqrt{Area_{Cell} \div \pi}}{Perimeter_{Cell}}$$

Shape change of cells over time is displayed using the temporal color coder plugin (developed by Kota Miura, Centre for Molecular and Cellular Imaging, EMBL Heidelberg, Germany) on the bare outlines of cell masks.

Wound healing assay

WT, RPTPγ-KO, and p22^{phox}-KO MCF7 cells were seeded onto fibronectin-coated (1.85 μg/cm^2) 24-well culture plates containing two-well silicone culture inserts (IBIDI) to create a cell-free gap. After the culture insert was removed, cells were stimulated either with H_2O_2 (0.5 mM) or with EGF-Alexa647 (1 or 160 ng/ml) and imaged immediately. Transmission images were acquired on the Leica SP8 confocal microscope with the environment-controlled chamber maintained at 37°C and 5% CO_2 using transmitted light of the white light laser and a 10×, 0.3NA air objective for 12 h at a time interval of 10′.

To analyze cell-migration, segmentation was performed using Trainable Weka Segmentation Plugin in Fiji (Arganda-Carreras *et al*, 2017). For each experiment, one image from the transmission stack was chosen to manually label the pixels in three classes: cell-free gap, inner part of the cells, and cell boundaries. Considering the best trade-off between precision and recall for a single class, Bayes Net Classifier was trained on the labeled data and then applied to the whole image stack to obtain masks for each class for the time series. The cell-count was quantified with MATLAB/Python by size thresholding the detected particles for noise removal, finding geometric centers of the objects, dividing every 512 × 512 image on 16 × 16 bins of size 32 × 32 pixels and calculating the number of cells in the constructed bin. The boundary bin position was detected via the largest drop of cell density on the first frame. The bins in the gap and in the bulk were defined with respect to the position of the initial gap boundary (Fig 6F: schematic in inset). The number of cells in indicated spatial bins were calculated at acquired temporal-frames (imaged at 10′ intervals) for each image-stacks and averaged over 4–5 experimental repeats.

Clonogenic assay

WT, RPTPγ-KO, and p22^{phox}-KO MCF7 cells were uniformly seeded in linear increment (100, 200 or 300 cells per well) in 6-well tissue culture plates (SARSTEDT), incubated at 37°C, 5% CO_2 in DMEM growth media supplemented with 2 mM L-Glutamine, 1% NEAA

and either 10% FBS or 0.5% FBS + 20 ng/ml EGF. The growth medium was exchanged every alternate day. After 7 days, the plates were washed with PBS, fixed with 4% (v/v in PBS) PFA (EM-grade, EMS) for 10′ and stained with 0.05% (v/v in PBS) crystal violet (Sigma-Aldrich Biochemie GmbH) for 10′. The excess crystal violet was removed by washing three times with PBS. The lids were removed for 3–4 h to dry the plates before imaging. Plates were scanned on Typhoon TRIO$^+$ variable mode imager (GE Healthcare, Buckinghamshire, UK) with the following settings: Cy5 filter (ex. 633 nm, em. 670 band-pass and PMT 530), pixel size 50 μm, and focal plane +3 mm.

To quantify the occupied culture-well area by proliferated cell-colonies, the image of the scanned well was intensity thresholded for the pixels occupied by colonies and a binary mask was obtained. By using Analyze Particles command in Fiji (Schindelin *et al*, 2012), the area of the mask was calculated and normalized to the area of the culture well. For a given cell type, assuming the direct proportionality between the final cell number and the initial number of seeded cells, the final percent area occupied by the cell colonies was normalized by the factor of linear proportion (1, 2, or 3 for 100, 200, or 300 initial cells, respectively). Thereby, the percent occupied areas from all the treated culture-wells from an individual cell type were combined together for a given growth media condition.

Statistical analysis

Statistical analyses were performed with the test specified in the figure legends, with the number of independent experiments (N) and analyzed cells (n).

Computational modeling and data fitting

To capture the interactions between EGFR and the PTPs across the different conditions, the following model of differential equations was used, as schematized by the general symmetric autocatalytic toggle switch model in Fig 5A:

$$\frac{1}{\lambda_E}\frac{dEGFR_{p/T}}{dt} = EGFR_{np/T}\left(\varepsilon_1\, EGFR_{np/T} + \varepsilon_2\, EGF{-}EGFR_{np/T} + \alpha_1\, EGFR_{p/T} + \alpha_2\, EGF{-}EGFR_{p/T}\right) - \left(\gamma_1 \frac{RPTP\gamma_T}{EGFR_T}\right) RPTP\gamma_{A/T}\, EGFR_{p/T} - \left(\gamma_2 \frac{TCPTP_T}{EGFR_T}\right) EGFR_{p/T}$$

$$\frac{1}{\lambda_P}\frac{dRPTP\gamma_{A/T}}{dt} = RPTP\gamma_{Ox/T} - \left(\frac{\kappa_2}{\kappa_1}\right) RPTP\gamma_{A/T} - \left(\beta \frac{EGFR_T}{\kappa_1}\right) RPTP\gamma_{A/T}\left(EGFR_{p/T} + EGF{-}EGFR_{p/T}\right)$$

$$\frac{1}{\lambda_E}\frac{dEGF{-}EGFR_{\frac{np}{T}}}{dt} = EGF{-}EGFR_{\frac{np}{T}}\left(\varepsilon_3\, EGFR_{\frac{np}{T}} + \varepsilon_4\, EGF{-}EGFR_{\frac{np}{T}} + \alpha_3\, EGFR_{\frac{p}{T}} + \alpha_4\, EGF{-}EGFR_{\frac{p}{T}}\right) - \left(\gamma_3 \frac{RPTP\gamma_T}{EGFR_T}\right) RPTP\gamma_{\frac{A}{T}}\, EGF{-}EGFR_{\frac{p}{T}} - \left(\gamma_4 \frac{TCPTP_T}{EGFR_T}\right) EGF{-}EGFR_{p/T}$$

Here, $EGFR_{p/T}$, $RPTP\gamma_{A/T}$, and $EGF{-}EGFR_{p/T}$ describe the fractions of active (phosphorylated) proteins, relative to the respective total protein concentration, while $EGFR_{np/T} = 1 - \frac{EGF-EGFR_T}{EGFR_T} - EGFR_{p/T}$, $PTP_{Ox/T} = 1 - PTP_{A/T}$ and $EGF{-}EGFR_{np/T} = \frac{EGF-EGFR_T}{EGFR_T} - EGF{-}EGFR_{p/T}$ describe the fractions of inactive (non-phosphorylated or oxidized) proteins, where $\frac{EGF-EGFR_T}{EGFR_T}$ is the fraction of liganded EGFR molecules that is provided as an input parameter, analogous to the experimental procedure. Parameters $\varepsilon_1{-}\varepsilon_4$ and $\alpha_1{-}\alpha_4$ represent the different rate constants in the second-order phosphorylation reactions (Fig EV4A) of the non-phosphorylated EGFR species ($EGFR_{np}$ and $EGF{-}EGFR_{np/T}$). These EGFR activation parameters are assumed to be dependent on the properties of EGFR only; therefore, their values are shared across the different conditions, while the remaining parameters on the right side (with the exception for k_2/k_1, which depends on the intrinsic properties of RPTPγ only) are fitted in condition-specific manner, i.e., they differ between the conditions according to the performed experimental perturbations. The rest of the rate constants depict: γ_1 and γ_3 – second-order RPTPγ-specific dephosphorylation, γ_2 and γ_4 – second-order (TC)PTP-dependent dephosphorylation, k_2/k_1 – intrinsic PTP deactivation/activation ratio, β – second-order EGFR-dependent oxidation. Parameters $EGFR_T$, $RPTP\gamma_T$, and $TCPTP_T$ depict the respective total protein concentrations, they appear due to the normalization procedure, where active protein concentrations are mapped to active fractions by dividing with the total protein concentrations. The bracketed parameter groups ($\Gamma_1 = \gamma_1 \frac{RPTP\gamma_T}{EGFR_T}$; $\Gamma_2 = \gamma_2 \frac{TCPTP_T}{EGFR_T}$; $\Gamma_3 = \gamma_3 \frac{RPTP\gamma_T}{EGFR_T}$; $\Gamma_4 = \gamma_4 \frac{TCPTP_T}{EGFR_T}$; $B = \beta \frac{EGFR_T}{k_1}$; $k_{21} = \frac{k_2}{k_1}$) were estimated as single parameters during the fitting procedure, and the ones containing protein concentrations were allowed to vary according to the respective experimental conditions, typically involving protein knockout or rescue perturbations (see table in Fig EV4B). Values of Γ_1, Γ_3, and B were estimated in an unshared fashion for perturbations of RPTPγ expression (B was set to zero for the knockout condition), values of Γ_2 and Γ_4 were also estimated separately for the perturbations of TCPTP expression, while $\Gamma_1{-}\Gamma_4$, and B values were estimated separately for the WT condition where the EGFR expression differed. Parameters λ_E ($EGFR_T$) and λ_P (κ_1) appear due to the normalization procedure (to generate fractions of active proteins), they only contribute to the relative kinetics and do not affect the steady state values, hence they were not estimated.

For a given parameter set and condition, a bifurcation profile was calculated depicting the dependence of the fraction of phosphorylated EGFR ($EGFR_{p/T} + EGF{-}EGFR_{p/T}$) on the input fraction of EGF-bound EGFR ($\frac{EGF-EGFR_T}{EGFR_T}$) in steady state, using a custom-made continuation algorithm. The resulting profiles were compared (using sum-of-squares) with the corresponding dose–response dependencies from the experimental data points of the respective condition (Fig EV4C; each blue circle is measured steady state $\alpha_L{-}\alpha_p$ dependency in a cell or western blot for a given dose; offsets were removed except for the conditions with pre-activation). Finally, using these comparisons for all conditions as a cost function, a custom-made Metropolis Hastings algorithm was employed to perform iterative parameter estimation of all the parameters (shared and non-shared) together, until no marked improvement of the cost function was detected.

Subsequently, bifurcation diagrams were generated depicting the dependence of the fraction of phosphorylated EGFR ($EGFR_{p/T} + EGF{-}EGFR_{p/T}$) on the RPTP$\gamma$-dependent dephosphorylation rate $\Gamma_1 = \left(\gamma_1 \frac{RPTP\gamma_T}{EGFR_T}\right)$ for multiple different values of fraction of EGF-

bound EGFR ($\frac{EGF-EGFR_T}{EGFR_T}$), to compile the 3D bifurcation surfaces (Fig 5G–I). The corresponding dose–response profiles were overlayed (red lines) on these surfaces at the previously estimated Γ_1 values and are matching the profiles shown in Fig 5G–I.

All data fitting procedures and bifurcation diagram calculations were performed using a custom-made code in MATLAB (MATLAB and Statistics Toolbox Release R2022a, The MathWorks, Inc., Natick, MA, USA).

Data availability

All data is available in the figures and source data files. Correspondence and request for materials should be addressed to Philippe IH Bastiaens. pSpCas9(BB)-2A-GFP (PX458) (Addgene plasmid # 48138) plasmids require a material transfer agreement from Addgene. The custom code used for global fitting of the dose response data is available in a github repository under the link: https://github.com/astanoev/EGFR-PTP-Dynamics

Expanded View for this article is available online.

Acknowledgements
We would like to thank Dr. A. Krämer for critically reading the manuscript, M. Reichl for cell culture work, and Dr. M. Schulz for FACS (all at Systemic Cell Biology, MPI for Molecular Physiology). We thank Dr. C. Sorio, Department of Pathology, University of Verona, Verona, Italy for the generous gift of rabbit anti-RPTPγ. The project was partly funded by the European Research Council (ERC AdG 322637) to PIHB. Open Access funding enabled and organized by Projekt DEAL.

Author contributions
Maitreyi S Joshi: Formal analysis; investigation; visualization; methodology; writing – original draft. **Angel Stanoev:** Software; formal analysis; investigation; visualization; methodology. **Birga Soetje:** Formal analysis; visualization; methodology. **Jan Huebinger:** Formal analysis; investigation; visualization; methodology; writing – original draft; writing – review and editing. **Veronika Zorina:** Formal analysis; visualization; methodology. **Lisaweta Roßmannek:** Methodology. **Kirsten Michel:** Methodology. **Philippe IH Bastiaens:** Conceptualization; formal analysis; supervision; funding acquisition; investigation; visualization; methodology; writing – original draft; project administration; writing – review and editing. **Sven AH Müller:** Methodology.

Disclosure and competing interests statement
The authors declare that they have no conflict of interest.

References

Alvarado D, Klein DE, Lemmon MA (2010) Structural basis for negative cooperativity in growth factor binding to an EGF receptor. *Cell* 142: 568–579

Ambasta RK, Kumar P, Griendling KK, Schmidt HHHW, Busse R, Brandes RP (2004) Direct interaction of the novel Nox proteins with p22phox is required for the formation of a functionally active NADPH oxidase. *J Biol Chem* 279: 45935–45941

Arganda-Carreras I, Kaynig V, Rueden C, Eliceiri KW, Schindelin J, Cardona A, Seung HS (2017) Trainable Weka segmentation: a machine learning tool for microscopy pixel classification. *Bioinformatics* 33: 2424–2426

Bae YS, Kang SW, Seo MS, Baines IC, Tekle E, Chock PB, Rhee SG (1997) Epidermal growth factor (EGF)-induced generation of hydrogen peroxide. *J Biol Chem* 272: 217–221

Barr AJ, Ugochukwu E, Lee WH, King ONF, Filippakopoulos P, Alfano I, Savitsky P, Burgess-Brown NA, Müller S, Knapp S (2009) Large-scale structural analysis of the classical human protein tyrosine Phosphatome. *Cell* 136: 352–363

Basolo F, Serra C, Ciardiello F, Fiore L, Russo J, Campani D, Dolei A, Squartini F, Toniolo A (1992) Regulation of surface-differentiation molecules by epidermal growth factor, transforming growth factor alpha, and hydrocortisone in human mammary epithelial cells transformed by an activated c-ha-ras proto-oncogene. *Int J Cancer* 51: 634–640

Bastiaens PIH, Squire A (1999) Fluorescence lifetime imaging microscopy: spatial resolution of biochemical processes in the cell. *Trends Cell Biol* 9: 48–52

Baumdick M, Brueggemann Y, Schmick M, Xouri G, Sabet O, Davis L, Chin JW, Bastiaens PIH (2015) EGF-dependent re-routing of vesicular recycling switches spontaneous phosphorylation suppression to EGFR signaling. *Elife* 4: e12223

Baumdick M, Gelléri M, Uttamapinant C, Beránek V, Chin JW, Bastiaens PIH (2018) A conformational sensor based on genetic code expansion reveals an autocatalytic component in EGFR activation. *Nat Commun* 9: 3847

Beechem JM (1992) Global analysis of biochemical and biophysical data. *Methods Enzymol* 210: 37–54

Birk D, Gansauge F, Gansauge S, Formentini A, Lucht A, Beger HG (1999) Serum and correspondent tissue measurements of epidermal growth factor (EGF) and epidermal growth factor receptor (EGF-R): clinical relevance in pancreatic cancer and chronic pancreatitis. *Int J Pancreatol* 25: 89–96

Brüggemann Y, Karajannis LS, Stanoev A, Stallaert W, Bastiaens PIH (2021) Growth factor–dependent ErbB vesicular dynamics couple receptor signaling to spatially and functionally distinct Erk pools. *Sci Signal* 14: eabd9943

Cappiello F, Casciaro B, Mangoni ML (2018) A novel in vitro wound healing assay to evaluate cell migration. *J Vis Exp* 2018: 10–15

Charafe-Jauffret E, Ginestier C, Monville F, Finetti P, Adélaïde J, Cervera N, Fekairi S, Xerri L, Jacquemier J, Birnbaum D *et al* (2006) Gene expression profiling of breast cell lines identifies potential new basal markers. *Oncogene* 25: 2273–2284

Chung I, Akita R, Vandlen R, Toomre D, Schlessinger J, Mellman I (2010) Spatial control of EGF receptor activation by reversible dimerization on living cells. *Nature* 464: 783–787

Cohen S, Carpenter G, King L (1980) Epidermal growth factor-receptor-protein kinase interactions. Co-purification of receptor and epidermal growth factor-enhanced phosphorylation activity. *J Biol Chem* 255: 4834–4842

Cool DE, Tonks NK, Charbonneau H, Walsh KA, Fischer EH, Krebs EG (1989) cDNA isolated from a human T-cell library encodes a member of the protein-tyrosine-phosphatase family. *Proc Natl Acad Sci USA* 86: 5257–5261

De Melker AA, Van Der Horst G, Calafat J, Jansen H, Borst J (2001) C-Cbl ubiquitinates the EGF receptor at the plasma membrane and remains receptor associated throughout the endocytic route. *J Cell Sci* 114: 2167–2178

Denu JM, Tanner KG (1998) Specific and reversible inactivation of protein tyrosine phosphatases by hydrogen peroxide: evidence for a sulfenic acid intermediate and implications for redox regulation. *Biochemistry* 37: 5633–5642

Fischer EH, Charbonneau H, Tonks NK (1991) Protein tyrosine phosphatases: a diverse family of intracellular and transmembrane enzymes. *Science* 253: 401–406

Grecco HE, Roda-Navarro P, Verveer PJ (2009) Global analysis of time correlated single photon counting FRET-FLIM data. *Opt Express* 17: 6493–6508

Grecco HE, Roda-Navarro P, Girod A, Hou J, Frahm T, Truxius DC, Pepperkok R, Squire A, Bastiaens PIH (2010) In situ analysis of tyrosine phosphorylation networks by FLIM on cell arrays. *Nat Methods* 7: 467–472

Grecco HE, Roda-Navarro P, Fengler S, Bastiaens PIH (2011) High-throughput quantification of posttranslational modifications in situ by CA-FLIM. *Methods Enzymol* 500: 37–58

Haglund K, Shimokawa N, Szymkiewicz I, Dikic I (2002) Cbl-directed monoubiquitination of CIN85 is involved in regulation of ligand-induced degradation of EGF receptors. *Proc Natl Acad Sci USA* 99: 12191–12196

Haj FG, Verveer PJ, Squire A, Neel BG, Bastiaens PIH (2002) Imaging sites of receptor dephosphorylation by PTP1B on the surface of the endoplasmic reticulum. *Science* 295: 1708–1711

Haj FG, Sabet O, Kinkhabwala A, Wimmer-Kleikamp S, Roukos V, Han HM, Grabenbauer M, Bierbaum M, Antony C, Neel BG *et al* (2012) Regulation of signaling at regions of cell-cell contact by endoplasmic reticulum-bound protein-tyrosine phosphatase 1B. *PLoS ONE* 7: e36633

Hajdu T, Váradi T, Rebenku I, Kovács T, Szöllösi J, Nagy P (2020) Comprehensive model for epidermal growth factor receptor ligand binding involving conformational states of the extracellular and the kinase domains. *Front Cell Dev Biol* 8: 1–16

Hancock JF, Paterson H, Marshall CJ (1990) A polybasic domain or palmitoylation is required in addition to the CAAX motif to localize p21ras to the plasma membrane. *Cell* 63: 133–139

Herbst JJ, Opresko LK, Walsh BJ, Lauffenburger DA, Wiley HS (1994) Regulation of postendocytic trafficking of the epidermal growth factor receptor through endosomal retention. *J Biol Chem* 269: 12865–12873

Hino N, Rossetti L, Marín-Llauradó A, Aoki K, Trepat X, Matsuda M, Hirashima T (2020) ERK-mediated mechanochemical waves direct collective cell polarization. *Dev Cell* 53: 646–660

Hiratsuka T, Fujita Y, Naoki H, Aoki K, Kamioka Y, Matsuda M (2015) Intercellular propagation of extracellular signal-regulated kinase activation revealed by in vivo imaging of mouse skin. *Elife* 4: e05178

Huebinger J, Grecco H, Masip ME, Christmann J, Fuhr GR, Bastiaens PIH (2021) Ultrarapid cryo-arrest of living cells on a microscope enables multiscale imaging of out-of-equilibrium molecular patterns. *Sci Adv* 7: 1–13

Ichinose J, Murata M, Yanagida T, Sako Y (2004) EGF signalling amplification induced by dynamic clustering of EGFR. *Biochem Biophys Res Commun* 324: 1143–1149

Imai Y, Leung CKH, Friesen HG, Shiu RPC (1982) Epidermal growth factor receptors and effect of epidermal growth factor on growth of human breast cancer cells in long-term tissue culture. *Cancer Res* 42: 4394–4398

Jacinto E, Facchinetti V, Liu D, Soto N, Wei S, Jung SY, Huang Q, Qin J, Su B (2006) SIN1/MIP1 maintains rictor-mTOR complex integrity and regulates Akt phosphorylation and substrate specificity. *Cell* 127: 125–137

Jagnandan D, Church JE, Banfi B, Stuehr DJ, Marrero MB, Fulton DJR (2007) Novel mechanism of activation of NADPH oxidase 5: calcium sensitization via phosphorylation. *J Biol Chem* 282: 6494–6507

Joh T, Itoh M, Katsumi K, Yokoyama Y, Takeuchi T, Kato T, Wada Y, Tanaka R (1986) Physiological concentrations of human epidermal growth factor in biological fluids: use of a sensitive enzyme immunoassay. *Clin Chim Acta* 158: 81–90

Juhasz A, Ge Y, Markel S, Chiu A, Matsumoto L, van Balgooy J, Roy K, Doroshow JH (2009) Expression of NADPH oxidase homologues and accessory genes in human cancer cell lines, tumours and adjacent normal tissues. *Free Radic Res* 43: 523–532

Kawahara T, Ritsick D, Cheng G, Lambeth JD (2005) Point mutations in the proline-rich region of p22phox are dominant inhibitors of Nox1- and Nox2-dependent reactive oxygen generation. *J Biol Chem* 280: 31859–31869

Klein CH, Truxius DC, Vogel HA, Harizanova J, Murarka S, Martín-Gago P, Bastiaens PIH (2019) PDEδ inhibition impedes the proliferation and survival of human colorectal cancer cell lines harboring oncogenic KRas. *Int J Cancer* 144: 767–776

Koseska A, Bastiaens PIH (2020) Processing temporal growth factor patterns by an epidermal growth factor receptor network dynamically established in space. *Annu Rev Cell Dev Biol* 36: 359–383

LaForgia S, Morse B, Levy J, Barnea G, Cannizzaro LA, Li F, Nowell PC, Boghosian-Sell L, Glick J, Weston A *et al* (1991) Receptor protein-tyrosine phosphatase γ is a candidate tumor suppressor gene at human chromosome region 3p21. *Proc Natl Acad Sci USA* 88: 5036–5040

Laine RF, Tosheva KL, Gustafsson N, Gray RDM, Almada P, Albrecht D, Risa GT, Hurtig F, Lindås AC, Baum B *et al* (2019) NanoJ: a high-performance open-source super-resolution microscopy toolbox. *J Phys D Appl Phys* 52: 163001

Lammers R, Bossenmaier B, Cool DE, Tonks NK, Schlessinger J, Fischer EH, Ullrich A (1993) Differential activities of protein tyrosine phosphatases in intact cells. *J Biol Chem* 268: 22456–22462

Lemmon MA, Bu Z, Ladbury JE, Zhou M, Pinchasi D, Lax I, Engelman DM, Schlessinger J (1997) Two EGF molecules contribute additively to stabilization of the EGFR dimer. *EMBO J* 16: 281–294

Levkowitz G, Waterman H, Zamir E, Kam Z, Oved S, Langdon WY, Beguinot L, Geiger B, Yarden Y (1998) c-Cb1/Sli-1 regulates endocytic sorting and ubiquitination of the epidermal growth factor receptor. *Genes Dev* 12: 3663–3674

Lin S, Hirayama D, Maryu G, Matsuda K, Hino N, Deguchi E, Aoki K, Iwamoto R, Terai K, Matsuda M (2022) Redundant roles of EGFR ligands in the ERK activation waves during collective cell migration. *Life Sci Alliance* 5: 1–13

Liou J, Kim ML, Won DH, Jones JT, Myers JW, Ferrell JE, Meyer T (2005) STIM is a Ca2+ sensor essential for Ca2+–store- depletion-triggered Ca2+ influx. *Curr Biol* 15: 1235–1241

Liu P, Cleveland TE IV, Bouyain S, Byrne PO, Longo PA, Leahy DJ (2012) A single ligand is sufficient to activate EGFR dimers. *Proc Natl Acad Sci USA* 109: 10861–10866

Low-Nam ST, Lidke KA, Cutler PJ, Roovers RC, Van Bergen En Henegouwen PMP, Wilson BS, Lidke DS (2011) ErbB1 dimerization is promoted by domain co-confinement and stabilized by ligand binding. *Nat Struct Mol Biol* 18: 1244–1249

Masip ME, Huebinger J, Christmann J, Sabet O, Wehner F, Konitsiotis A, Fuhr GR, Bastiaens PIH (2016) Reversible cryo-arrest for imaging molecules in living cells at high spatial resolution. *Nat Methods* 13: 665–672

Meng TC, Fukada T, Tonks NK (2002) Reversible oxidation and inactivation of protein tyrosine phosphatases in vivo. *Mol Cell* 9: 387–399

Offterdinger M, Georget V, Girod A, Bastiaens PIH (2004) Imaging phosphorylation dynamics of the epidermal growth factor receptor. *J Biol Chem* 279: 36972–36981

Ogiso H, Ishitani R, Nureki O, Fukai S, Yamanaka M, Kim JH, Saito K, Sakamoto A, Inoue M, Shirouzu M *et al* (2002) Crystal structure of the complex of human epidermal growth factor and receptor extracellular domains. *Cell* 110: 775–787

Ostman A, Böhmer F (2001) Regulation of receptor tyrosine kinase signaling by protein tyrosine phosphatases. *Trends Cell Biol* 11: 258–266

Paulsen CE, Truong TH, Garcia FJ, Homann A, Gupta V, Leonard SE, Carroll KS (2012) Peroxide-dependent sulfenylation of the EGFR catalytic site enhances kinase activity. *Nat Chem Biol* 8: 57–64

Ran FA, Hsu PD, Wright J, Agarwala V, Scott DA, Zhang F (2013) Genome engineering using the CRISPR-Cas9 system. *Nat Protoc* 8: 2281–2308

Reynolds AR, Tischer C, Verveer PJ, Rocks O, Bastiaens PIH (2003) EGFR activation coupled to inhibition of tyrosine phosphatases causes lateral signal propagation. *Nat Cell Biol* 5: 447–453

Rhee SG (1999) Redox signaling: hydrogen peroxide as intracellular messenger. *Exp Mol Med* 31: 53–59

Rhee SG, Kang SW, Jeong W, Chang TS, Yang KS, Woo HA (2005) Intracellular messenger function of hydrogen peroxide and its regulation by peroxiredoxins. *Curr Opin Cell Biol* 17: 183–189

Rich T, Zhao F, Cruciani RA, Cella D, Manola J, Fisch MJ (2017) Association of fatigue and depression with circulating levels of proinflammatory cytokines and epidermal growth factor receptor ligands: a correlative study of a placebo-controlled fatigue trial. *Cancer Manag Res* 9: 1–10

Roos W, Fabbro D, Kung W, Costa SD, Eppenberger U (1986) Correlation between hormone dependency and the regulation of epidermal growth factor receptor by tumor promoters in human mammary carcinoma cells. *Proc Natl Acad Sci USA* 83: 991–995

Rostovtsev VV, Green LG, Fokin VV, Sharpless KB (2002) A stepwise huisgen cycloaddition process: copper(I)-catalyzed regioselective 'ligation' of azides and terminal alkynes. *Angew Chem Int Ed Engl* 41: 2596–2599

Rowinsky EK (2004) The erbB family: targets for therapeutic development against cancer and therapeutic strategies using monoclonal antibodies and tyrosine kinase inhibitors. *Annu Rev Med* 55: 433–457

Salazar-Cavazos E, Nitta CF, Mitra ED, Wilson BS, Lidke KA, Hlavacek WS, Lidke DS (2020) Multisite EGFR phosphorylation is regulated by adaptor protein abundances and dimer lifetimes. *Mol Biol Cell* 31: 695–708

Sato K, Sato A, Aoto M, Fukumi Y (1995) c-Src phosphorylates epidermal growth factor receptor on tyrosine 845. *Biochem Biophys Res Commun* 215: 1078–1087

Schindelin J, Arganda-Carreras I, Frise E, Kaynig V, Longair M, Pietzsch T, Preibisch S, Rueden C, Saalfeld S, Schmid B *et al* (2012) Fiji: an open-source platform for biological-image analysis. *Nat Methods* 9: 676–682

Schmick M, Vartak N, Papke B, Kovacevic M, Truxius DC, Rossmannek L, Bastiaens PIH (2014) KRas localizes to the plasma membrane by spatial cycles of solubilization, trapping and vesicular transport. *Cell* 157: 459–471

Seger R, Ahn NG, Boulton TG, Yancopoulos GD, Panayotatos N, Radziejewska E, Ericsson L, Bratlien RL, Cobb MH, Krebs EG (1991) Microtubule-associated protein 2 kinases, ERK1 and ERK2, undergo autophosphorylation on both tyrosine and threonine residues: implications for their mechanism of activation. *Proc Natl Acad Sci USA* 88: 6142–6146

Shan Y, Eastwood MP, Zhang X, Kim ET, Arkhipov A, Dror RO, Jumper J, Kuriyan J, Shaw DE (2012) Oncogenic mutations counteract intrinsic disorder in the EGFR kinase and promote receptor dimerization. *Cell* 149: 860–870

Sheardown H, Cheng YL (1996) Tear EGF concentration following corneal epithelial wound creation. *J Ocul Pharmacol Ther* 12: 239–243

Sibilia M, Kroismayr R, Lichtenberger BM, Natarajan A, Hecking M, Holcmann M (2007) The epidermal growth factor receptor: from development to tumorigenesis. *Differentiation* 75: 770–787

Sonntag MH, Ibach J, Nieto L, Verveer PJ, Brunsveld L (2014) Site-specific protection and dual labeling of human epidermal growth factor (hEGF) for targeting, imaging, and cargo delivery. *Chemistry* 20: 6019–6026

Sorio C, Mendrola J, Lou Z, LaForgia S, Croce CM, Huebner K (1995) Characterization of the receptor protein tyrosine phosphatase gene product PTPγ: binding and activation by Triphosphorylated nucleosides. *Cancer Res* 55: 4855–4864

Soubeyran P, Kowanetz K, Szymkiewicz I, Langdon WY, Dikic I (2002) Cbl-CIN85-endophilin complex mediates ligand-induced downregulation of EGF receptors. *Nature* 416: 183–187

Stallaert W, Brüggemann Y, Sabet O, Baak L, Gattiglio M, Bastiaens PIH (2018) Contact inhibitory Eph signaling suppresses EGF-promoted cell migration by decoupling EGFR activity from vesicular recycling. *Sci Signal* 11: eaat0114

Stanoev A, Mhamane A, Schuermann KC, Grecco HE, Stallaert W, Baumdick M, Brüggemann Y, Joshi MS, Roda-Navarro P, Fengler S *et al* (2018) Interdependence between EGFR and phosphatases spatially established by vesicular dynamics generates a growth factor sensing and responding network. *Cell Syst* 7: 295–309

Stanoev A, Nandan AP, Koseska A (2020) Organization at criticality enables processing of time-varying signals by receptor networks. *Mol Syst Biol* 16: 1–13

Stringer C, Wang T, Michaelos M, Pachitariu M (2021) Cellpose: a generalist algorithm for cellular segmentation. *Nat Methods* 18: 100–106

Tiganis T (2002) Protein tyrosine phosphatases: dephosphorylating the epidermal growth factor receptor. *IUBMB Life* 53: 3–14

Tischer C, Bastiaens PIH (2003) Lateral phosphorylation propagation: an aspect of feedback signalling? *Nat Rev Mol Cell Biol* 4: 971–975

Van Niekerk CC, Poels LG (1999) Reduced expression of protein tyrosine phosphatase gamma in lung and ovarian tumors. *Cancer Lett* 137: 61–73

Vanlandingham PA, Ceresa BP (2009) Rab7 regulates late endocytic trafficking downstream of multivesicular body biogenesis and cargo sequestration. *J Biol Chem* 284: 12110–12124

Verveer PJ, Squire A, Bastiaens PIH (2000a) Global analysis of fluorescence lifetime imaging microscopy data. *Biophys J* 78: 2127–2137

Verveer PJ, Wouters FS, Reynolds AR, Bastiaens PIH (2000b) Quantitative imaging of lateral ErbB1 receptor signal propagation in the plasma membrane. *Science* 290: 1567–1570

Vieira AV, Lamaze C, Schmid SL (1996) Control of EGF receptor signaling by clathrin-mediated endocytosis. *Science* 274: 2086–2089

Woo HA, Yim SH, Shin DH, Kang D, Yu DY, Rhee SG (2010) Inactivation of peroxiredoxin I by phosphorylation allows localized H_2O_2 accumulation for cell signaling. *Cell* 140: 517–528

Yarden Y, Schlessinger J (1987) Self-phosphorylation of epidermal growth factor receptor: evidence for a model of intermolecular allosteric activation. *Biochemistry* 26: 1434–1442

Yu FSX, Yin J, Xu K, Huang J (2010) Growth factors and corneal epithelial wound healing. *Brain Res Bull* 81: 229–235

Yudushkin IA, Schleifenbaum A, Kinkhabwala A, Neel BG, Schultz C, Bastiaens PIH (2007) Live-cell imaging of enzyme-substrate interaction reveals spatial regulation of PTP1B. *Science* 315: 115–119